Lithological, petrophysical and seal properties of mass-transport complexes (MTCs), northern Gulf of Mexico

Nan Wu[1], Christopher A-L. Jackson[1], Howard D. Johnson[1], David M. Hodgson[2]

[1]Basins Research Group, Department of Earth Science & Engineering, Imperial College, Prince Consort Road, London, SW7 2BP, UK

[2]School of Earth and Environment, University of Leeds, Leeds, LS2 9JT, UK

*Email: n.wu16@imperial.ac.uk

Acknowledgements

We thank PGS, in particular Don Herron and Scott Opdyke, for providing the subsurface dataset and allowing the publication of the paper. The first author thank China Scholarship Council for providing financial support. We would also thank Harya Nugraha and Michael Steventon who helped us throughout the work. We thank the editor, Dr. Barry J. Katz, who handled our manuscript, and Dr. Andrew S. Madof and Dr. Derek Sawyer for thorough reviews and positive feedback that significantly improve the manuscript.

Abstract

Mass transport complexes (MTCs) are one of the most sedimentologically and seismically distinctive depositional elements in deep-water depositional systems. Seismic reflection data provide spectacular images of their structure, size, and distribution, although a lack of borehole data means there is limited direct calibration between MTC lithology and petrophysical expression, or knowledge of how they may act as hydrocarbon reservoir seals. In this study, we evaluate the lithological and petrophysical properties, and seismic characteristics of three deeply-buried (>2300 m/7546 ft below the seabed), Pleistocene MTCs in the northern Gulf of Mexico. We show that: (i) MTC lithology is highly variable, comprising a mudstone-rich debrite matrix containing large (4.5 km^3/1.08 mi^3), deformed, sandstone-rich blocks; (ii) MTCs are generally acoustically faster and are more resistive than lithologically similar (i.e. mudstone-dominated) slope deposits occurring at a similar burial depth; (iii) MTC velocity and resistivity increase with depth, likely reflecting an overall downward increase in the degree of compaction; and (iv) the lowermost 15-30 m (49-98 ft) of the MTCs, which represent the basal shear zones, are characterised by relatively high P-wave velocity and resistivity values, likely due to shear-induced over-compaction. We conclude that detailed analysis of petrophysical data, in particular velocity and resistivity logs, may allow recognition of MTCs in the absence of high-quality seismic reflection data, including explicit identification of the basal shear zone. Furthermore, the relatively thick basal shear zone, rather than the overlying and substantially thicker MTC itself, may form the primary permeability barrier and thus seal for underlying hydrocarbon accumulations.

1 Introduction

Mass-transport complexes (MTCs) comprise deposits from a range of weakly turbulent to fully cohesive, plug-like sediment gravity flows such as slides, slumps, and debris-flows (Talling et al., 2012). MTCs are one of the most sedimentological and seismically distinctive depositional elements in deep-water depositional systems, where they may form a key component of the stratigraphic record (Posamentier and Martinsen, 2011). MTCs may represent geohazards, threatening seabed infrastructure, and can generate seabed topography that controls the dispersal of subsequent sediment gravity-currents (Martinsen, 1989; Hühnerbach and Masson, 2004; Solheim et al., 2005; Lee et al., 2007; Sawyer, 2007; Urgeles and Camerlenghi, 2013; Kneller et al., 2016). MTCs may also represent drilling hazards because of unpredictable intraformational pressures, and can slow down the penetration rate of suction anchor piles and jetted conductors, thus leading to non-productive time (Shipp et al., 2004). In addition, MTCs may form hydraulic seals to hydrocarbon accumulations hosted in underlying (or laterally equivalent) sandstone reservoirs (Piper et al., 1997; Shipp, 2004; Sawyer et al., 2009; Algar et al., 2011), or form reservoir themselves (Meckel III, 2011). The composition and distribution of MTCs, and our ability to recognise them in the subsurface, are thus of concern to the hydrocarbon industry.

Typically, MTCs are studied in the subsurface using seismic reflection data (e.g. Prather et al., 1998; Posamentier and Kolla, 2003; Frey Martinez et al., 2005; Posamentier, 2005; Moscardelli et al., 2006; Moscardelli and Wood, 2008; Bull et al., 2009; Moernaut and De Batist, 2011; Ortiz-Karpf et al., 2015; Ortiz‐Karpf et al., 2016), or in the field (e.g. Martinsen et al., 2003; Jackson and Johnson, 2009; Dykstra et al., 2011; King et al., 2011; Shipp et al., 2011; Alves, 2015; Sobiesiak et al., 2016; Hodgson et al., 2018). Seismic reflection data allow determination of the distribution, external geometry, internal structure, and kinematics of MTCs. However, these data do not provide a direct calibration of MTC lithology, which must instead be inferred from seismic facies analysis (Moscardelli et al., 2006; Madof et al., 2009; Perov and Bhattacharya, 2011). In contrast, field-based studies permit detailed analysis of MTC structure and lithology, but these exhumed and weathered systems do not permit a direct petrophysical characterisation. In addition, the field-based studies may not permit a fully three-dimensional analysis of very large (i.e. tens to several hundreds of metres thick, by several hundreds of kilometres in areal extent) MTCs, and/or may not reveal their basal and upper surfaces.

Integrated petrophysical and lithological studies of buried MTCs are relatively rare, typically drawing on data collected from shallowly buried (<1400 m/4593 ft) deposits (e.g. Sawyer, 2007; Flemings et al., 2008; Sawyer et al., 2009; Algar et al., 2011; Dugan, 2012). These studies show that MTCs can be very fine-grained, and may be acoustically faster (and thus more rigid) and have higher resistivity (and thus lower porosity) than surrounding, *in-situ* deep-water sediment of similar composition (Piper et al., 1997; Shipp, 2004; Sawyer, 2007; Algar et al., 2011; Dugan, 2012). How these properties vary with depth, and how deeply-buried MTCs are expressed in petrophysical data at depths of interest to the hydrocarbon industry, is poorly understood. An exception to this is presented by Algar et al. (2011), who used borehole data to study several deeply buried MTCs offshore NW Borneo; however, in this example they lacked access to high-resolution 3D seismic data to link seismic facies with lithology and petrophysical properties.

In this study, we use 3D seismic reflection and borehole data from the Atwater Valley protraction area of the northern Gulf of Mexico to investigate the relationship between the 3D seismic reflection and petrophysical expression of three deeply (1900 m- 3100 m) buried MTCs, especially the top and base surfaces of MTCs. By doing this, we can improve our ability to use such data to predict their subsurface rock properties and associated fluid flow behaviour.

2 Geological setting

Our study area is located in Block 8 of the Atwater Valley concession, c. 130 km (80.8 mi) SW of the modern Mississippi delta mouth, and c. 60 km (37.3 mi) basinward of the Pleistocene shelf edge (Galloway et al., 2000; Galloway, 2001) (Figure 1). Present water depths range from 1150 m (3773 ft) in the SE to 650 m (2133 ft) in the NW. The northern Mississippi slope comprises a series of salt diapirs and minibasins formed due to flow of the Jurassic Louann Salt (Martin and Bouma, 1982; Peel et al., 1995). This study focuses on Pleistocene sediments preserved within minibasins formed by subsidence into allochthonous salt (Jackson et al., 2018) (Figure 1). During the Early to Middle Pleistocene, the Mississippi River and its tributaries supplied the Mississippi delta, which delivered significant amounts of sediment to the shelf, slope, and basin-floor (Galloway et al., 2000; Galloway, 2008; Galloway et al., 2011). In the Late Pleistocene, the East Mississippi river merged with the Red River, forming a deeply incised, pro-glacial Mississippi valley (Saucier, 1997; Galloway et al., 2000). This valley, and the downdip Mississippi canyon, represented the main conduit for sediment transfer onto the basin floor (Weimer et al., 1998; Galloway et al., 2000; Winker and Booth, 2000).

A seabed map (Figure 2A) and a top salt depth map (Figure 2B) highlight the main salt structures and minibasins within the study area. This study focuses on the stratigraphic fill of an N-S trending, up to 21 km (13 mi) long and 10 km (6.2 mi) wide minibasin that contains a 3.5 km (2.2 mi) thick succession of Pleistocene siliciclastics (minibasin 5; Figure 2A and 2B). Biostratigraphic data provide relatively low-resolution age control for the Cenozoic sediments (Figure 3B).

3 Dataset and Methods

The seismic dataset was acquired in 1995-1998, and reprocessed as a single survey in 2008. It is a 3D zero-phase, Kirchhoff pre-stack depth-migrated seismic reflection volume, with a vertical sample rate of 10 m (32.8 ft), record length (depth) of 15 km (9.32 mi), and final bin size of 25 m x 25 m (82 ft x 82 ft). The dataset covers an area of approximately 550 km^2 (212.4 mi^2) in the southwestern Mississippi Canyon (MC) and northwestern Atwater Valley (AT) protraction areas of the east-central Gulf of Mexico (Figure 2). A downward increase and decrease in acoustic impedance is expressed as red (positive) and blue (negative) reflection events, respectively. The estimated vertical seismic resolution in the interval of interest ranges from 17-27 m (55.8-88.6 ft). A slightly deviated exploration well (AT-8 #1 ST) was drilled in 1997 in the east of the study area, encountering a c. 3600 m (11811 ft) thick succession of Pleistocene deep-water clastic succession (Figure 2) (see Jackson et al., 2018 for details of the biostratigraphic data). The well-log dataset includes measurements of velocity (Sonic), gamma-ray (GR) and resistivity (RT). Shale volume (Vsh) was calculated based on the GR response using the following equation:

$$\mathrm{Vsh} = \frac{\mathrm{GRlog} - \mathrm{GRmin}}{\mathrm{GRmax} - \mathrm{GRmin}}$$

P-wave velocity (Vp) was calculated based on the sonic (DT) response using the following equation:

$$\mathrm{Vp} = \frac{1}{\mathrm{Sonic}} * 10^6 \text{ m/s}$$

We mapped eight highly reflective (i.e. reflections picked on high amplitude peaks or troughs), laterally continuous seismic horizons (H0 to seabed; Figure 3B) that delineate several MTCs preserved in minibasin 5. The MTCs are imaged using a combination of geometric, amplitude and frequency based variance and chaos attributes. The variance attribute was calculated based on the Van Bemmel and Pepper (2000) edge detection method; this converts the amplitude-based seismic volume into a reflection discontinuity volume that is particularly useful for highlighting structural (e.g. faults) and stratigraphic (e.g. the abrupt seismic facies change from chaotic MTCs to more continuous slope strata). The chaos attribute was measured in using dip and azimuth estimation method; like variance, chaos highlights abrupt changes in seismic facies, and it was also used for mapping structural and stratigraphic discontinuities (Chopra and Marfurt, 2007; Brown, 2011; Koson et al., 2014).

Where available, we used density and sonic log data to generate a synthetic seismogram to tie seismic and borehole data. This allowed a direct assessment of the lithology and petrophysical properties of the MTCs, as well as their bounding strata. The horizons used for the QC are the salt weld horizon and a high amplitude peak above the salt weld (see supplementary martial 1). Because the calliper log is only available in the section below the salt weld, the hole conditions, and thus quality of the extracted log data in the interval of interest, can only be constrained using the ROP (rate of penetration) log (see supplementary material 2A). The ROP log is relatively smooth, suggesting the hole conditions and well-log data in the interval of interest are relatively good. For example, the ROP log is relatively smooth, increasing from 0.004 to 0.008 m/s from sea-level to 2750 m and 0.008 to 0.0125 m/s from 2750 m to 3800 m. This suggests that the hole conditions and well-log data in the interval of interest are relatively good. The overall trends seen are logically related to increasing burial compaction in the MTC intervals (see supplementary material 2B); and the variations characterising the BSZ occur over a short length-scale, and it seems unlikely that they all represent poor hole conditions at this specific depth.

Five MTC-bearing intervals were drilled and logged by AT-8 #1 ST; due to the lack of well data for the shallowest MTCs, we here analyse only three (Figure 3B). Well-log data (i.e., GR, Sonic and RT) were used to infer the lithology of the MTCs and their bounding strata. Cross-plots were constructed to examine the petrophysical-property variations within MTC-bearing intervals and bounding strata.

4 Seismic facies analysis

A regional N-S trending seismic profile through minibasin 5 illustrates the geometry of the depocentre and bounding salt structures (Figure 3A). We see two main seismic reflection configurations: (i) *chaotic*, which are interpreted as MTCs (i.e. remobilised strata); and (ii) *continuous*, which are interpreted as slope deposits (i.e. in-situ strata) (Figure 3C) (Prather et al., 1998; Roesink et al., 2004; Sincavage et al., 2004; Madof et al., 2009; Doughty-Jones et al., 2017). The seismic facies characteristics of the MTCs (facies 3.1 and 3.2) and slope deposits (facies 1 and 2) are further classified based on a more detailed analysis of their seismic reflection characteristics, and by comparing their expression (e.g. reflectivity and continuity, and their external and internal geometry) with previous seismic facies analysis schemes developed for age-equivalent (i.e. Plio-Pleistocene) deep-water sediments deposited in nearby areas (Prather et al., 1998; Sawyer et al., 2007; Madof et al., 2009). We here briefly describe the observed seismic facies and their GR expression (see also Table 1), before we provide a more detailed analysis of the petrophysical expression of the MTC-bearing intervals.

4.1 Seismic facies 1 (SF1)

SF1 comprises sub-parallel to parallel, moderate continuity, high-amplitude reflections. SF1 is c. 40-50 m (131-164 ft) thick, and has flat upper and lower contacts with bounding deposits (Table 1). SF1 has a blocky, low GR response at its base, and a serrated, higher GR response at its top, displaying an overall fining-upward trend. Based on its log response and previous seismic facies-based studies, we infer that SF1 represents thinly bedded, sandstone-rich (at its base) and mudstone-rich (at its top) deposits, possibly deposited in a channel-levee system or at the fringes of a lobe complex (Table 1). SF1 is thus comparable with C_{th} facies of Prather et al. (1998), with similar seismic facies being documented by Roesink et al. (2004), Sincavage et al. (2004), and Madof et al. (2009) (i.e. inter-bedded sandstone- and mudstone-rich turbidites).

4.2 Seismic facies 2 (SF2)

SF2 is c. 100-170 m (328.1-557.7 ft) thick, and is bounded by sub-parallel to parallel, relatively continuous, low-to-medium amplitude reflections. It comprises laterally continuous, parallel, low- to medium amplitude reflections (Table 1). SF2 displays a high GR response, suggesting it is mudstone-dominated. Based on its expression in seismic and borehole data, and by comparison to seismic facies interpreted in other studies, we infer SF2 represents low-energy, 'background-type' slope deposits, comprising mudstone-rich hemipelagic deposits that may be interbedded with very thin turbidites (Prather et al., 1998; Madof et al., 2009; Perov and Bhattacharya, 2011).

4.3 Seismic facies 3.1 (SF3.1)

SF3.1 is c. 150-180 m (492-590 ft) thick, has a rugose top surface and a flat base (Table 1), and comprises moderately deformed, folded and faulted, medium-to-high amplitude seismic reflections. SF3.1 is characterised by a bell-shaped GR response, with a fining upward trend near its bottom, and box-shaped, 80-120 m (262-393 ft) thick intervals of low GR at its middle and top. The lower part of SF3.1 is dominated by high GR intervals and is inferred to be mudstone-rich. In contrast, the middle and upper parts of SF3.1 are characterised by low GR values, and are inferred to be sandstone-rich, with thinly bedded sandstone and mudstone. The abundance of faulting and folding, combined with the rugose upper surface, suggest SF3.1 has been remobilised and transported, most likely within a MTC. Based its sandstone-rich character we propose that SF3.1 was originally deposited in and ultimately sourced from the remobilisation of, submarine lobes (Mahaffie, 1995; Prather et al., 1998; Posamentier and Kolla, 2003; Posamentier, 2005; Sawyer et al., 2007; Doughty-Jones et al., 2017).

4.3 Seismic facies 3.2 (SF3.2)

SF3.2 comprises c. 190-270 m (623-885 ft) thick packages of chaotic, low-to-moderate amplitude seismic reflections. The top of SF3.2 is rugose, whereas its basal contact is relatively flat (Table 1). SF3.2 is characterised by a serrated, overall high GR response that locally contains sharp-based, box-shaped, low GR intervals (Table 1). SF3.2 is therefore interpreted to be mudstone-dominated (i.e. high GR intervals) and more specifically, based on its seismic and log response, and interpretations arising from previous seismic facies-based studies (Prather et al., 1998; Sawyer, 2007; Madof et al., 2009; Perov and Bhattacharya, 2011), as a mudstone-rich debrite. Sandstone-rich intervals (i.e. low GR intervals) are inferred to be sandstone blocks encased within the very fin-grained debrite matrix.

5. Lithology and distribution of MTCs

We focus on three MTCs preserved in minibasin 5 (MTC1-3; Figure 3B, 3C), and we begin by providing a description of their general seismic expression and lithology. In subsequent sections we synthesize observations from these three MTCs to investigate their detailed petrophysical response, and how this relates to MTC structure and emplacement.

5.1 MTC 1

Geometry and seismic facies

MTC 1 is bound by horizon H1 and H2 (Figure 3B). It has a tongue-shaped external form, widening towards the SE, away from diapir A (Figure 4A, 4B). MTC 1 is up to 270 m (885 ft) thick, being thickest in the minibasin centre. A 180 m (590 ft) high, 6 km (3.7 mi) long erosion surface separates MTC 1 from an overlying debrite (SF3.2), and an underlying interval that contains folded and faulted blocks (Figure 4C, 4D). The abundance of faulting and folding, combined with scours along the basal surface (Figure 4C), suggest that large blocks were transported within MTC1. These blocks are defined by packages of SF3.1 and SF1 that are 80-180 m (262-590 ft) thick, 4.5-6.8 km (2.8-4.2 mi) long, and 2-3.6 km (1.2-2.2 mi) wide, and which contain NE-SW-striking thrusts. The well intersects the distal part of MTC 1, in a location where thrusts and folds occur (Figure 4A).

Lithology

MTC 1 is sandstone-rich (SF3.1) near its base and mudstone-rich (SF3.2) at its top (Figure 5A). To better investigate lithology variations associated with the three constituent seismic facies of MTC 1, we generated a cross-plot of shale volume (Vsh) and velocity (Vp) (Figure 5B).

This plot shows that: (1) both SF1 and SF3.1 is heterogeneous, containing both sandstone- and mudstone-rich intervals; SF3.1 contains minor amounts of muddy sandstone, whereas SF1 does not; (2) sandstone-rich deposits associated with SF1 and SF3.1 are capped and surrounded by mudstone-rich debrite, an observation also inferred from their seismic expression (Figure 4C, 4D); and (3) SF3.2 is mudstone-dominated, can be clearly differentiated from other seismic facies, and is defined by a relatively narrow distribution in the cross plot.

5.2 MTC 2

Geometry and seismic facies

We infer MTC 2 comprises two separate, debrite-dominated (i.e. SF3.2) deposits (MTC 2.1 and 2.2; Figure 6A, 6B), separated by a through-going seismic horizon H2.2 (Figure 6C, 6D). Taken together, MTC 2.1 and 2.2 define an up to 120 m (393.7 ft) thick, N-S trending, lenticular-shaped body that widens slightly northwards (Figure 6B). Two bodies in the centre of the minibasin have sharp, sub-vertical contacts with MTC 2.1, and are interpreted as remnant blocks (Figure 6C, 6D). The well interests the middle part of MTC 2, in a location where it is dominated by SF3.2 (Figure 6A).

Lithology

The remnant block is mudstone-rich at its base, and comprises sandstone and mudstone towards its top (Figure 7A). Overlying MTCs are mudstone-dominated (MTC 2.1 and 2.2; Figure 7A), although the lithological composition of MTC 2 varies when observed in the cross-plot of shale volume (Vsh) and velocity (Vp) (Figure 7B). For example: (1) SF1 and SF3.2 are mudstone-dominated, with a small portion of sandstone-rich deposits, although the former is more mudstone-rich than the latter; (2) SF2 is mudstone-rich, containing some muddy sandstone; and (3) sandstone-rich deposits associated with SF1 are capped and surrounded by mudstone-rich debrite and undeformed background deposits. A similar stratigraphic relationship is inferred from the seismic data (Figure 6C, 6D).

5.3 MTC 3

Geometry and seismic facies

MTC 3 occurs in the centre of the minibasin, is slightly elongate, and trends north (Figure 8A, 8B). MTC 3 is bounded by horizon H4 and H4.1 (Figure 3B), is up to 182 m (597 ft) thick, comprises chaotic, moderate-amplitude reflections (SF3.2), and has a flat base and rugose top (Figure 8C, 8D). The well intersects the central part of MTC 3, in a region where it is dominated by chaotic seismic facies (Figure 8A).

Lithology

MTC 3 has a mudstone-rich base and top, and a sandstone-rich middle (Figure 9A). The composition of MTC 3 is further revealed in a cross-plot of Vsh and Vp (Figure 9B). SF3.2 is dominated by sandstone-rich and mudstone-rich deposits, with a small proportion of muddy sandstone. The lithology of SF3.2 in MTC 3 is thus comparable to that observed in MTC 2, but different to that in MTC 1. Based on seismic and log data, MTC 3 is interpreted as a debrite-dominated MTC containing large, sandstone-rich (c. 70 m/229.7 ft in thickness) blocks.

6 Petrophysical analysis of MTCs

6.1 General variations in velocity and resistivity

Velocity (Vp) data from MTCs 1-3 show that: (i) MTCs are generally characterised by an overall downward increase in Vp (e.g. 2340-2487 m/7677-8159 ft, MTC3 in Figure 10A); (ii) mudstone-dominated parts of MTCs are acoustically faster than similar lithologies at similar burial depths (e.g. the mudstone-rich debrite in MTC 3 is acoustically faster than the overlying and underlying background mudstone-rich deposits; 2300-2550 m/7545.9-8366 ft in Figure 10A); (iii) sandstone-dominated parts of all three MTCs tend to have a relatively low Vp, and are acoustically slower than the overlying and underlying mudstone-rich debrite (see below); (iv) the uppermost 8-15 m (26-49 ft) of the MTCs, which are dominated by mudstone-rich sediments and directly underlie the top surface, are 3%-5% acoustically faster than similar material within the overlying background deposits (Figure 10A); and (v) the lowermost 15-30 m (49-98 ft) of the MTCs, which are invariably mudstone-dominated and which directly overlie the seismically defined base of the MTC, are 5%-9% and 7-25% acoustically faster than similar material within the overlying MTCs and underlying background deposits, respectively.

The reasons for the sharp increase in Vp just above the MTC basal shear surface is discussed further below.

Resistivity (RT) log data show that: (i) RT increases downward within MTCs, but decreases downward in lithologically similar slope deposits in bounding intervals (e.g. increases from 2770-2890 m/9087.9-9481.6 ft in MTC2, and decreases from 2890-3080 m/9481.6-10104.9 ft in the underlying remnant block, Figure 10B); (ii) mudstone-rich debrite (SF3.2) are typically more resistive than surrounding, undeformed background deposits at similar burial depths (e.g., 3075-3100 m/ 10088.6- 10170.6 ft in MTC1 Figure 10B); (iii) sandstone-dominated parts of all three MTCs tend to have a relatively low RT, and are less resistive than overlying and underlying mudstone-rich debrite (see below); (iv) RT response within MTC 2 and MTC 3 are lower than surrounding, undeformed, background deposits; (v) the uppermost 8-15 m (26-49 ft) MTCs 1 and 2 are characterised by RT values 30%-45% higher than overlying background deposits; and (vi) the lowermost 15-30 m (49-98 ft) of the MTCs are characterised by RT values that are 15%-25% higher than would be expected by the downward-increasing, 'background' RT trend response in the overlying MTC, and 16%-30% higher than underlying and thus more deeply buried, slope background deposits (Figure 14). This finding is consistent with previous studies that suggest that RT increases with depth within MTCs (Shipp, 2004; Dugan, 2012), but is counter to other studies which suggest MTCs are typically more resistive than surrounding sediments (Sawyer et al., 2009; Algar et al., 2011). We explore the reasons for this further in the discussion.

6.2 Petrophysical and acoustic characteristics of the basal shear zone and the top surface

The term basal shear surface (BSS) is defined by (Varnes, 1978) as a discrete seismic reflection defining the base of a relatively chaotic package of seismic reflections (i.e. an MTC). They infer this is the surface across which the MTC was translated and ultimately deposited, containing deformation associated with both these processes (see also Frey Martinez et al., 2005; Bull et al., 2009). In our study, the BSS is characterised by high-amplitude, negative seismic reflection that defines a downward decrease in acoustic impedance and, we infer, a change from acoustically fast MTC-related materials and the pre-MTC slope substrate. Field suggest that, rather than representing a discrete surface, the BSS identified in seismic reflection data instead defines a zone of deformed materials related to MTC transport and emplacement (basal shear zone or 'BSZ' of Hodgson et al., 2018, or 'kinematic boundary layer' of Butler et al., 2016). In detail, the BSZ comprises sediments deformed: (i) wholly within the MTC body during its transport and emplacement; (ii) wholly below the MTC within the pre-emplacement seabed, with strain imposed by shear caused by the overlying travelling mass; or (iii) within and below the travelling mass.

Our petrophysical data allow us to identify a 15-30 m thick zone define by relatively high VP and RT at the base of the MTCs. We interpret this interval represents the basal BSZ. These petrophysically defined zones are represented in seismic data by a seemingly discrete surface due to the limited vertical resolution of the latter (e.g. the 15 m thick BSZ of MTC 1 is only represented by a single trough reflection in seismic data). We propose that the BSZ could represent sediments that wholly within the MTCs, deposited at the lowermost section which has highest VP and RT response.

The BSSs of all three MTCs are all characterised by negative, medium-to-high amplitude seismic reflections of moderate continuity (Figure 4D, 6C, 8C). For example, the BSZ of MTC 1 is more reflective (i.e. -15701 at point a1 in Figure 11A) than the laterally correlative reflection within flanking background strata (i.e. -4008 at point b1 in Figure 11A). The top surfaces of all three MTCs are characterised by positive, medium-to-high amplitude seismic reflections of poor continuity (Figure 4C, 6C, 8C). For example, the reflection defining the top surface of MTC 1 is at point a2 in Figure 11B is more reflective (i.e. amplitude value of +22387) than the laterally correlative, weaker (-12408), negative amplitude reflection within flanking background strata (i.e. point b2 in Figure 11B).

Because amplitude (i.e. reflectivity) is a function of the reflection coefficient (RC) (i.e. acoustic impedance or 'AI' contrasts) and, ultimately, the acoustic properties of rocks, we can explore what lithological combination and/or variations in their physical properties (e.g. compaction) might give rise to the observed seismic response (equation 1):

$$RC = \frac{AI2 - AI1}{AI2 + AI1} \quad (1)$$

Where AI1 and AI2 are the sediments overlying and underlying the top surface and the BSZ of MTC 1, respectively (Figure 11C). Because the top surface and the BSZ of MTC 1 are more consolidated, they are acoustically faster and more resistive than the overlying and underlying undeformed deposits (i.e. the units directly above and below MTC1 are seismically 'softer') (See Figure 10A, 10B). AI is a function of acoustic velocity (Vp) and density (ρb) (equation 2):

$$AI = Vp * \rho b \quad (2)$$

Based on this, $AI_2 > AI_1$ across the top surface of MTC 1, and $AI_1 > AI_2$ across the BSZ of MTC 1. This illustrates why: (i) the top surface of MTC 1 is defined by a positive amplitude reflection, whereas the laterally correlative surface, encased within undeformed background deposits, is defined by a negative polarity reflection; and (ii) the amplitude of the BSZ of MTC 1 is not only defined by negative polarity, but is also brighter than that of the laterally correlative, undeformed background deposits.

6.3 Petrophysical and acoustic characteristics of sandstone-rich deposit within MTCs

MTC 1 has the thickest sandstone-rich interval (c. 170 m/557.7 ft). Sandstone-rich intervals within MTC 2.1, 2.2 and 3 are up to 30 m (98 ft), 10 m (32 ft) and 70 m (229 ft) thick, respectively (Table 2).

Overall, in contrast to mudstone-rich parts of MTCs where Vp and RT broadly increase with depth (Figure 12A), sandstone-rich parts of MTCs have variable depth trends (Figure 12B). The sandstone-rich parts of three MTCs have lower average Vp and RT values than the underlying and overlying mudstone-rich debrite (Figure 13). For example, the average Vp value for the sandstone-rich part of MTC 2 is 2140 m/s (7020.9 ft/s). This is lower than the average Vp values of the overlying and underlying mudstone-rich debrites, which are 2210 m/s (7250.7 ft/s) and 2240 m/s (7349.1 ft/s), respectively (Fig 13B). The sandstone-rich part of MTC 3 displays an overall increase in Vp and RT with depth (Figure 13A), although the sandstone-rich part of MTC 1 does not vary (Figure 13C).

The petrophysical properties of sandstone-rich parts of MTC 1 are different to those of surrounding mudstone-rich debrite and sandstone-rich deposits in overlying, undeformed background deposits (Figure 13 C). A simplified Vp depth trend can be proposed based on the observed Vp depth trend in Figure 10A. The MTC intervals, except the sandstone-rich blocks in MTC 1, tend to have relatively high Vp response compared to the overlying and underlying background slope deposits (see also Figure 12A, 12B), which typically exceed the inferred compaction trend. This suggests that MTC intervals, or at least their mudstone-rich sections, are more compacted than and perhaps overcompacted relative to overlying and underlying background slope deposits (Figure 12A). Within MTC 1, the Vp trend of the sandstone-rich blocks shifts sharply to a constant low Vp response as compared to the overlying mudstone-rich debrite that has increasing Vp with depth. This indicates that the sandstone-rich blocks of MTC 1 are *less* compacted than the mudstone-rich, debritic matrix. Furthermore, sandstone-rich blocks are only weakly resistive when compared to the overlying mudstone-rich units (Figure 10, Figure 12, Figure 13C). This may suggest that the sandstone-rich blocks in MTC 1 retain higher porosity and are water-saturated. However, because the MTCs are strongly heterogeneous, the general trends that we describe/interpret in this study may not be specifically tested in this case without a more detailed understanding of the specific consolidation profiles of the muddy vs. sandy lithologies.

7 Discussion

We have characterised: (i) the lithology of relatively deeply buried, seismic-scale MTCs; (ii) the relationship between MTC seismic facies and lithology; and (iii) the petrophysical properties of MTCs, and how they vary with depth and structural position within individual MTCs. Here, we discuss the key implications of our study.

7.1 Lithology of MTCs

In this study, we demonstrate that significant amounts of sandstone may be present within MTCs. This sandstone can be surprisingly thick (c. 170 m/557.7 ft), being contained in relatively homogeneous transported blocks (SF3.2), or relatively thin (10-30 m/32.8-98.4 ft), occurring interbedded with mudstone in remobilised lobe and/or channel-fill successions (Table 2). This compositional variability may reflect the different provenance of the MTCs; i.e. from mudstone-rich outer-shelves or slopes lacking sand, or from similar positions that are sandstone-rich due to the presence of deltas or previously deposited, deep-water channel-fills and lobes. MTCs are likely transported along the slope and being laterally bounded by salt diapirs. This contrasts with the widespread occurrence of argillaceous MTCs, such as those encountered in the Nankai Trough (e.g. Strasser et al., 2012), offshore Angola (e.g. Sikkema and Wojcik, 2000) and the Gulf of Mexico (e.g. Shipp, 2004; Flemings et al., 2005; Sawyer et al., 2007; Meckel III, 2011).

7.2 Petrophysical properties of MTCs

General Petrophysical properties

Prior well-log based studies from IODP and ODP drilling in the Northern Gulf of Mexico (Shipp et al., 2004; Sawyer, 2007; Sawyer et al., 2009; Dugan, 2012; Flemings et al., 2012) and Northwest Borneo (Algar et al., 2011) show that MTCs tend to have a higher Vp, density and RT values than surrounding non-MTC intervals. This reflects the fact that MTCs are more consolidated than their bounding sediments, an observation that is consistent with geotechnical measurements that indicate shear strength increases, whereas water content and void ratio decrease downward within MTCs (Piper et al., 1997; Shipp et al., 2004; Strong, 2009; Long et al., 2011; Alves et al., 2014). Physical experiments and theoretical models (e.g. consolidation, fluid-dynamics, and soil-mechanics) confirm that MTCs are denser than bounding strata, typically being densest within their basal shear zone (Major and Iverson, 1999; Sassa et al., 2003; Dugan and Germaine, 2008; Strong, 2009; Meissl et al., 2010).

We demonstrate that the three MTCs studied here are more compacted than surrounding background deposits, and that Vp, RT broadly increase downward, and at a higher rate than within underlying and overlying undeformed background sediments. Our findings are thus consistent with observations from Sawyer et al. (2009) and Algar et al. (2011), who show similar downward increase in Vp and RT within individual MTCs. However, RT values are lower than in underlying and overlying undeformed background sediments, except near the MTC basal shear zone. This observation is contrary to previous studies (Shipp, 2004; Sawyer et al., 2009; Dugan, 2012). We note, however, that these authors studied mudstone-dominated MTCs at relatively shallow burial depths (<1400 m/4593 ft), whereas those presented here are relatively sandstone-rich and lie at substantially greater burial depths (>2300 m/7546 ft). The differences observed between these studies may therefore reflect differences in the burial depth and lithology of MTC intervals studied.

Insights into emplacement processes; basal shear surface or zone?

Experimental models show that debrites are typically deposited in response to top-down ‘freezing’ of weakly turbulent, plug-like laminar flows; because the lower parts of these flows are the last to stop deforming they may be more strained (Pickering and Hiscott, 2015). Thin section and outcrop-based studies show evidence of liquefaction and fluidization related structures in the lower part of MTC intervals (Ogata et al., 2014). In this study, we show that the lower 15-30 m (49-98 ft) of the studied MTCs are characterised by relatively high Vp and RT when compared to overlying and underlying deposits. Petrophysical data suggest that, rather than being underlain by a basal shear *surface*, the MTCs overlie a basal shear *zone* (BSZ). BSZ thickness and infer strain (based on Vp value) appears to be positively correlated to the thickness of the overlying MTCs; i.e. the thicker the MTCs, the thicker and more strained the BSZs. For example, MTC 3 and MTC 2 are 170 m (557.7 ft) and 83 m (272 ft) thick, with 30 m

(98 ft) and 26 m (85 ft) thick BSZs, respectively. Vp values sharply increase at the BSZs by around 20-25% for each MTC, as compared to the overlying debritic sediments of the main MTC body. This contrasts with MTC 1, where the BSZ is only 15 m (49 ft) thick and where Vp increases by only 7%. These differences in Vp may reflect the fact that the well penetrates: (i) different parts of the different MTCs (i.e. the debritic margin of MTC 1 vs. the debritic centre of MTCs 2 and 3), and (ii) different internal elements of the MTCs (i.e. transported blocks in MTC 1 vs. debris flow matrix in MTCs 2 and 3).

Only one well is available for this analysis; however, we can make some observations regarding the lateral variability of petrophysical properties (i.e. Vp and RT) within the three studied MTCs. Vp and the thickness of the BSZs appear to vary laterally, being highest beneath the main body of an MTC (i.e. MTC 2 and MTC 3), and lowest in more distal parts (i.e. MTC 1). This suggests that within a single MTC, the BSZ might be thinnest along its thin margins and thickest beneath its thick centre. However, the thickness and pore pressure of the BSZ might be controlled by other factors, such as: (i) slope angle, which would dictate the momentum of MTCs towards the underlying substrate (i.e. the steeper slope angle, the higher the momentum, and *vice versa* (Algar et al., 2011); (ii) the thickness of the overlying MTC (i.e. BSZ thickness is proportional to the thickness of the overlying MTCs; e.g., MTC 3 is thicker than MTC2, and thus the thickness of BSZ of the former is thicker than that of the latter; (iii) MTC content; the MTCs with fewer blocks (i.e. MTC 2 and 3) will have a thicker BSZs than the MTCs with more transported blocks (MTC 1); (iv) the lithology of the substrate; i.e. a ductile, mudstone-rich substrate may be highly sheared, with the shear stress from the overlying MTCs leading to dewatering rather than erosion of the BSZ (Alves and Lourenço, 2010; Ortiz-Karpf et al., 2017); and (v) bathymetric confinement, which would influence the substrate geometry, heterogeneity, internal characteristics and pathway of MTCs; the thickness of MTCs and their BSZ would thus vary laterally (Ortiz-Karpf et al., 2017).

In detail, we suggest the inferred high shear strain characterising the BSZs can be captured in a three-stage, MTC emplacement model (Figure 14a, b): (i) Phase 1 – high shear stresses within the BSZs cause an increase in fluid pressure beneath the rapidly deposited very fine-grained upper part of the flow; this drives liquefaction within the BSZ (Figure 14c); (ii) Phase 2 – continued shearing drives fluidization and pore fluid expulsion (Figure 14d); and (iii) Phase 3 - as gravity induced shear stress progresses, fluid escape continues, resulting in pore space reduction and BSZ compaction (Figure 14e). A key observation is that, even where 30 m (98 ft) thick, the BSZs are too thin to be recognised in seismic reflection data (i.e. these intervals are sub-seismic).

Identifying MTCs using petrophysical data

On the middle to lower slope of the Mississippi Fan, GR log data cannot differentiate between MTCs and undeformed background deposits because both are mudstone-rich (i.e. both are characterised by serrated, overall high-GR responses). In this situation, Vp and RT logs may be more useful, as they may present higher values in the MTC debritic matrix than the background deposits, principally because these deposits have undergone some degree of transport, and thus emplacement-related strain and compaction. Our method, which may allow well-based, petrophysically driven mapping of MTCs and their BSZs, can be used in lower-quality 3D seismic datasets that image deep-water sedimentary successions (e.g. sub-salt-canopy minibasins within which seismic resolution is relatively low).

7.3 Petroleum implication of MTCs

MTCs as hydrocarbon seals

Most petrophysics-based studies of MTCs indicate these deposits are dominated by mudstone. Furthermore, these studies suggest that, because they are over-compacted, these mudstone-rich MTCs may be better seals than surrounding deposits (Algar et al., 2011). This study suggests that emplacement-related over-compaction in MTCs occurs within the BSZ, meaning this interval may have higher sealing potential than lithologically similar background deposits occurring at similar burial depths. The highly reflective nature of the BSZ of an MTC, which relates to its higher density and acoustic velocity, may thus be an indicator of higher sealing potential. The mudstone-rich debrite in the upper part of MTC 1 appears to be a good top and lateral seal for the underlying folded and faulted sandstone-rich transported blocks (Figure 4C, 4D). In MTC 2, the mudstone-rich debrite (MTC 2.1 and MTC 2.2) and the corresponding BSZ may act as a good top and lateral seal for the underlying, sandstone-rich parts of the remnant block (Figure 6C, 6D). In the BSZ of MTC 3, which appears to be the most consolidated of all the recognised BSZs, could act as good base seal for underlying sandstone-rich deposits.

Reservoir potential

In this study, we show that sandstone-rich transported blocks can be up to c. 180 m (590 ft) thick, 6800 m (22309 ft) long, cover 2.5 km^2 (0.95 mi^2) in map-view, and have an approximate volume of 4.5 km^3/1.1 mi^3 (i.e. MTC 1). The sandstone-rich parts within remnant blocks underlying MTC 2 are up to 20 m (65 ft) thick, cover 0.0145 km^2 (0.006 mi^2) in map-view, and have an approximate volume of 0.29 km^3 (0.07 mi^3). Petrophysical data indicate the sandstone-rich blocks within MTC 1 and in the remnant block might be under-pressured and may thus be characterised by relatively high porosities. These transported yet less-deformed sandstone-rich blocks (i.e. MTC 1), and the sandstone-rich parts within the remnant blocks under MTC 2, could be potential reservoirs and may thus be of interest to the hydrocarbon industry (Moore et al., 1995; Alves, 2010; Dunlap et al., 2010; Principaud et al., 2015). In addition and as stated above, the sandstone-rich parts within MTC 1 and the remnant blocks are capped by the overlying mudstone-rich deposit, and are externally sealed by the surrounding, mudsstone-rich background strata. Intra-MTC blocks of comparable size to those described here (i.e. 1-10 km/0.6-6 mi long, 0.3-2 km/0.18-1.2 mi wide, 50-500 m/164-1640 ft thick, and covering an area of 3.63-4 km^2/1.4-1.5 mi^2) have been described by other workers (e.g.,Moscardelli et al., 2006; Ogiesoba and Hammes, 2012).

Drilling hazards

Typically, MTCs are more consolidated than surrounding sediments and could slow down the penetration rate (i.e. Shipp, 2004). Therefore, MTCs are a major concern when designing suction anchor piles and jetted conductors (Newlin, 2003). In this study, the identification of the most consolidated BSZs from petrophysical data of MTCs could provide information for the design of the jetted conductors and suction anchor pile. Neglecting the presence of BSZs might cause unexpected problems during the penetration of MTCs (i.e. increase drilling time and costly rig). In addition, we use the amplitude attribute to infer the petrophysical properties of MTCs. The high amplitude nature of BSZs of MTCs could provide information on identification the most consolidated section of MTCs.

8. Conclusions

We use seismic reflection and well-log data to study the seismic and petrophysical expression, and lithology of three MTCs preserved in a deep-water minibasin, northern Gulf of Mexico. We show that: (i) MTCs are dominated by chaotic, medium-to-low amplitude seismic reflections (debrite), and packages of deformed, but more continuous, medium-to-high amplitude reflections (remnant and transported blocks); (ii) MTCs are mudstone-dominated, whereas the transported and remnant blocks are relatively sandstone-rich; (iii) MTCs are characterised by high acoustic velocities (as revealed by Vp data) and are relatively more resistive relative to surrounding background sediments at similar burial depths; (iv) the top surface of the MTCs are characterised by a positive seismic reflection and the base shear surface (BSS) is characterised by a negative seismic reflection; (v) the lowermost 15-30 m (49-98 ft) of the MTCs define basal shear zones, which are characterised by relatively high P-wave velocity (Vp) and resistivity (RT) values due to shear-induced over-compaction; (v) Vp and RT vary laterally within the BSZs, being higher below the thicker, main body of MTC than towards the lateral margins; (vi) the hydrocarbon seal potential of MTCs may be internally highly variable, with the BSZ displaying the greatest seal capacity (smallest pore throat diameter and lowest permeability) below the main body of the MTCs compared to the deposit margins; and (vii) sandstone-rich blocks within the MTC 1 tend to be under-compacted and may maintain anomalously high porosities. Sandstone-rich blocks also tend to be internally sealed by overlying mudstone-rich debris and externally sealed by background mudstone-rich deposits.

Reference

Algar, S., C. Milton, H. Upshall, J. Roestenburg, and P. Crevello, 2011, Mass-transport deposits of the deepwater northwestern Borneo margin (Malaysia)—Characterization from seismic-reflection, borehole, and core data with implications for hydrocarbon exploration and exploitation: Mass-transport deposits in deepwater settings: Tulsa, Oklahoma, SEPM Special Publication, v. 96, p. 351-366.

Alves, T. M., 2010, 3D seismic examples of differential compaction in mass-transport deposits and their effect on post-failure strata: Marine Geology, v. 271, p. 212-224.

Alves, T. M., 2015, Submarine slide blocks and associated soft-sediment deformation in deep-water basins: a review: Marine and Petroleum Geology, v. 67, p. 262-285.

Alves, T. M., K. Kurtev, G. F. Moore, and M. Strasser, 2014, Assessing the internal character, reservoir potential, and seal competence of mass-transport deposits using seismic texture: A geophysical and petrophysical approach: AAPG bulletin, v. 98, p. 793-824.

Alves, T. M., and S. D. Lourenço, 2010, Geomorphologic features related to gravitational collapse: Submarine landsliding to lateral spreading on a late Miocene–Quaternary slope (SE Crete, eastern Mediterranean): Geomorphology, v. 123, p. 13-33.

Brown, A. R., 2011, Interpretation of three-dimensional seismic data, Society of Exploration Geophysicists and American Association of Petroleum Geologists.

Bull, S., J. Cartwright, and M. Huuse, 2009, A review of kinematic indicators from mass-transport complexes using 3D seismic data: Marine and Petroleum Geology, v. 26, p. 1132-1151.

Butler, R. W., J. T. Eggenhuisen, P. Haughton, and W. D. McCaffrey, 2016, Interpreting syndepositional sediment remobilization and deformation beneath submarine gravity flows; a kinematic boundary layer approach: Journal of the Geological Society, v. 173, p. 46-58.

Chopra, S., and K. J. Marfurt, 2007, Seismic attributes for prospect identification and reservoir characterization, Society of Exploration Geophysicists and European Association of Geoscientists and Engineers.

Doughty-Jones, G., M. Mayall, and L. Lonergan, 2017, Stratigraphy, facies, and evolution of deep-water lobe complexes within a salt-controlled intraslope minibasin: AAPG Bulletin, v. 101, p. 1879-1904.

Dugan, B., 2012, Petrophysical and consolidation behavior of mass transport deposits from the northern Gulf of Mexico, IODP Expedition 308: Marine Geology, v. 315, p. 98-107.

Dugan, B., and J. T. Germaine, 2008, Near - seafloor overpressure in the deepwater Mississippi Canyon, northern Gulf of Mexico: Geophysical Research Letters, v. 35.

Dunlap, D. B., L. J. Wood, C. Weisenberger, and H. Jabour, 2010, Seismic geomorphology of offshore Moroccos east margin, Safi Haute Mer area: AAPG bulletin, v. 94, p. 615-642.

Dykstra, M., K. Garyfalou, V. Kertznus, B. Kneller, J. Milana, M. Molinaro, M. Szuman, and P. Thompson, 2011, Mass-transport deposits: combining outcrop studies and seismic forward modeling to understand lithofacies distributions, deformation, and their seismic expression: Mass-Transport Deposits. SEPM, Tulsa, OK.

Flemings, P., H. Long, B. Dugan, J. Germaine, C. John, J. H. Behrmann, D. Sawyer, and I. Expedition, 2008, Pore pressure penetrometers document high overpressure near the seafloor where multiple submarine landslides have occurred on the continental slope, offshore Louisiana, Gulf of Mexico: Earth and Planetary Science Letters, v. 269, p. 309-325.

Flemings, P. B., I. Behrmann, T. Davies, C. John, and E. Team, 2005, Gulf of Mexico hydrogeology—Overpressure and fluid flow processes in the deepwater Gulf of Mexico: Slope stability, seeps, and shallow-water flow: Integrated Ocean Drilling Program Scientific Prospectus, v. 308, p. 1-52.

Flemings, P. B., C. John, and J. Behrmann, 2012, Expedition 308 synthesis: overpressure, consolidation, and slope stability on the continental slope of the Gulf of Mexico.

Frey Martinez, J., J. Cartwright, and B. Hall, 2005, 3D seismic interpretation of slump complexes: examples from the continental margin of Israel: Basin Research, v. 17, p. 83-108.

Galloway, W. E., 2001, Cenozoic evolution of sediment accumulation in deltaic and shore-zone depositional systems, northern Gulf of Mexico Basin: Marine and Petroleum Geology, v. 18, p. 1031-1040.

Galloway, W. E., 2008, Depositional evolution of the Gulf of Mexico sedimentary basin: Sedimentary basins of the world, v. 5, p. 505-549.

Galloway, W. E., P. E. Ganey-Curry, X. Li, and R. T. Buffler, 2000, Cenozoic depositional history of the Gulf of Mexico basin: AAPG bulletin, v. 84, p. 1743-1774.

Galloway, W. E., T. L. Whiteaker, and P. Ganey-Curry, 2011, History of Cenozoic North American drainage basin evolution, sediment yield, and accumulation in the Gulf of Mexico basin: Geosphere, v. 7, p. 938-973.

Hodgson, D., H. Brooks, A. Ortiz-Karpf, Y. Spychala, D. Lee, and C.-L. Jackson, 2018, Entrainment and abrasion of megaclasts during submarine landsliding and their impact on flow behaviour: Geological Society, London, Special Publications, v. 477, p. SP477. 26.

Hühnerbach, V., and D. Masson, 2004, Landslides in the North Atlantic and its adjacent seas: an analysis of their morphology, setting and behaviour: Marine Geology, v. 213, p. 343-362.

Jackson, C. A.-L., Y. Zhang, D. A. Herron, and P. J. Fitch, 2018, Subsurface expression of a tertiary salt weld, Gulf of Mexico: Petroleum Geoscience, p. petgeo2018-008.

Jackson, C. A., and H. D. Johnson, 2009, Sustained turbidity currents and their interaction with debrite-related topography; Labuan Island, offshore NW Borneo, Malaysia: Sedimentary Geology, v. 219, p. 77-96.

King, P. R., B. R. Ilg, M. Arnot, G. H. Browne, L. J. Strachan, M. Crundwell, K. Helle, R. Shipp, P. Weimer, and H. Posamentier, 2011, Outcrop and seismic examples of mass-transport deposits from a late Miocene deep-water succession, Taranaki Basin, New Zealand: Mass-transport deposits in deepwater settings: Society for Sedimentary Geology (SEPM) Special Publication 96, p. 311-347.

Kneller, B., M. Dykstra, L. Fairweather, and J. P. Milana, 2016, Mass-transport and slope accommodation: implications for turbidite sandstone reservoirs: AAPG Bulletin, v. 100, p. 213-235.

Koson, S., P. Chenrai, and M. Choowong, 2014, Seismic attributes and their applications in seismic geomorphology: Bulletin of Earth Sciences of Thailand, v. 6, p. 1-9.

Lee, H. J., J. Locat, P. Desgagnés, J. D. Parsons, B. G. McAdoo, D. L. Orange, P. Puig, F. L. Wong, P. Dartnell, and E. Boulanger, 2007, Submarine mass movements on continental margins, Continental margin sedimentation: from sediment transport to sequence stratigraphy, v. 37, Citeseer, p. 213-274.

Long, H., P. Flemings, J. Germaine, and D. Saffer, 2011, Consolidation and overpressure near the seafloor in the Ursa Basin, Deepwater Gulf of Mexico: Earth and Planetary Science Letters, v. 305, p. 11-20.

Madof, A. S., N. Christie-Blick, and M. H. Anders, 2009, Stratigraphic controls on a salt-withdrawal intraslope minibasin, north-central Green Canyon, Gulf of Mexico: Implications for misinterpreting sea level change: AAPG bulletin, v. 93, p. 535-561.

Mahaffie, M., 1995, Reservoir classification for turbidite intervals at the Mars discovery, Mississippi Canyon Block 807, Gulf of Mexico.

Major, J. J., and R. M. Iverson, 1999, Debris-flow deposition: Effects of pore-fluid pressure and friction concentrated at flow margins: Geological Society of America Bulletin, v. 111, p. 1424-1434.

Martin, R. G., and A. H. Bouma, 1982, Active diapirism and slope steepening, northern Gulf of Mexico continental slope: Marine Georesources & Geotechnology, v. 5, p. 63-91.

Martinsen, O., 1989, Styles of soft-sediment deformation on a Namurian (Carboniferous) delta slope, Western Irish Namurian Basin, Ireland: Geological Society, London, Special Publications, v. 41, p. 167-177.

Martinsen, O. J., T. Lien, R. G. Walker, and J. D. Collinson, 2003, Facies and sequential organisation of a mudstone-dominated slope and basin floor succession: the Gull Island Formation, Shannon Basin, Western Ireland: Marine and Petroleum Geology, v. 20, p. 789-807.

Meckel III, L., 2011, Reservoir characteristics and classification of sand-prone submarine mass-transport deposits: SEPM Special Publication, v. 96, p. 432-452.

Meissl, S., J. Behrmann, and J. H. Behrmann, 2010, Data report: preliminary assessment of Pleistocene sediment strength in the Ursa Basin (Gulf of Mexico continental slope) from triaxial and ring shear test data: Proceedings of the Integrated Ocean Drilling Program.

Moernaut, J., and M. De Batist, 2011, Frontal emplacement and mobility of sublacustrine landslides: results from morphometric and seismostratigraphic analysis: Marine Geology, v. 285, p. 29-45.

Moore, J. G., W. B. Bryan, M. H. Beeson, and W. R. Normark, 1995, Giant blocks in the South Kona landslide, Hawaii: Geology, v. 23, p. 125-128.

Moscardelli, L., and L. Wood, 2008, New classification system for mass transport complexes in offshore Trinidad: Basin Research, v. 20, p. 73-98.

Moscardelli, L., L. Wood, and P. Mann, 2006, Mass-transport complexes and associated processes in the offshore area of Trinidad and Venezuela: AAPG bulletin, v. 90, p. 1059-1088.

Newlin, J., 2003, Suction Anchor Piles for the Na Kika FDS Mooring System Part 2: Installation Performance, Deepwater mooring systems: Concepts, design, analysis, and materials, p. 55-75.

Ogata, K., J. Mountjoy, G. A. Pini, A. Festa, and R. Tinterri, 2014, Shear zone liquefaction in mass transport deposit emplacement: A multi-scale integration of seismic reflection and outcrop data: Marine Geology, v. 356, p. 50-64.

Ogiesoba, O., and U. Hammes, 2012, Seismic interpretation of mass-transport deposits within the upper Oligocene Frio Formation, south Texas Gulf Coast: AAPG bulletin, v. 96, p. 845-868.

Ortiz-Karpf, A., D. Hodgson, and W. McCaffrey, 2015, The role of mass-transport complexes in controlling channel avulsion and the subsequent sediment dispersal patterns on an active margin: the Magdalena Fan, offshore Colombia: Marine and Petroleum Geology, v. 64, p. 58-75.

Ortiz-Karpf, A., D. M. Hodgson, C. A.-L. Jackson, and W. D. McCaffrey, 2017, Influence of Seabed Morphology and Substrate Composition On Mass-Transport Flow Processes and Pathways: Insights From the Magdalena Fan, Offshore Colombia: Journal of Sedimentary Research, v. 87, p. 189-209.

Ortiz ‐ Karpf, A., D. M. Hodgson, C. A. L. Jackson, and W. D. McCaffrey, 2016, Mass ‐ Transport Complexes as Markers of Deep ‐ Water Fold ‐ and ‐ Thrust Belt Evolution: Insights from the Southern Magdalena Fan, Offshore Colombia: Basin Research.

Peel, F., C. Travis, and J. Hossack, 1995, Genetic structural provinces and salt tectonics of the Cenozoic offshore US Gulf of Mexico: A preliminary analysis.

Perov, G., and J. P. Bhattacharya, 2011, Pleistocene shelf-margin delta: Intradeltaic deformation and sediment bypass, northern Gulf of Mexico: AAPG bulletin, v. 95, p. 1617-1641.

Pickering, K., and R. Hiscott, 2015, Deep Marine Systems: Processes, Deposits, Environments, Tectonic and Sedimentation, John Wiley & Sons.

Piper, D., C. Pirmez, P. Manley, D. Long, R. Flood, W. Normark, and W. Showers, 1997, Mass-transport deposits of the Amazon Fan: PROCEEDINGS-OCEAN DRILLING PROGRAM SCIENTIFIC RESULTS, p. 109-146.

Posamentier, H. W., 2005, Stratigraphy and geomorphology of deep-water mass transport complexes based on 3D seismic data, SEG Technical Program Expanded Abstracts 2005, Society of Exploration Geophysicists, p. 2300-2303.

Posamentier, H. W., and V. Kolla, 2003, Seismic geomorphology and stratigraphy of depositional elements in deep-water settings: Journal of sedimentary research, v. 73, p. 367-388.

Posamentier, H. W., and O. J. Martinsen, 2011, The character and genesis of submarine mass-transport deposits: insights from outcrop and 3D seismic data: Mass-transport deposits in deepwater settings: Society for Sedimentary Geology (SEPM) Special Publication 96, p. 7-38.

Prather, B. E., J. R. Booth, G. S. Steffens, and P. A. Craig, 1998, Classification, lithologic calibration, and stratigraphic succession of seismic facies of intraslope basins, deep-water Gulf of Mexico: AAPG bulletin, v. 82, p. 701-728.

Principaud, M., T. Mulder, H. Gillet, and J. Borgomano, 2015, Large-scale carbonate submarine mass-wasting along the northwestern slope of the Great Bahama Bank (Bahamas): Morphology, architecture, and mechanisms: Sedimentary Geology, v. 317, p. 27-42.

Roesink, J. G., P. Weimer, and R. Bouroullec, 2004, Sequence stratigraphy of Miocene to Pleistocene sediments of east-central Mississippi canyon, northern Gulf of Mexico.

Sassa, S., J. Miyamoto, and H. Sekiguchi, 2003, The dynamics of liquefied sediment flow undergoing progressive solidification, Submarine Mass Movements and Their Consequences, Springer, p. 95-102.

Saucier, R. T., 1997, Geomorphology and Quarternary Geologic History of the Lower Mississippi Valley. Volume 1.

Sawyer, D. E., 2007, Lateral Variations in Core, Log, and Seismic Attributes of a Mass Transport Complex in the Ursa Region, IODP Expedition 308, Northern Gulf of Mexico.

Sawyer, D. E., P. B. Flemings, B. Dugan, and J. T. Germaine, 2009, Retrogressive failures recorded in mass transport deposits in the Ursa Basin, Northern Gulf of Mexico: Journal of Geophysical Research: Solid Earth, v. 114.

Sawyer, D. E., P. B. Flemings, R. C. Shipp, and C. D. Winker, 2007, Seismic geomorphology, lithology, and evolution of the late Pleistocene Mars-Ursa turbidite region, Mississippi Canyon area, northern Gulf of Mexico: AAPG bulletin, v. 91, p. 215-234.

Shipp, R. C., 2004, Physical Characteristics and Impact of Mass Transport Complexes on Deepwater Jetted Conductors and Suction Anchor Piles.

Shipp, R. C., J. A. Nott, and J. A. Newlin, 2004, Physical characteristics and impact of mass transport complexes on deepwater jetted conductors and suction anchor piles: Offshore Technology Conference.

Shipp, R. C., P. Weimer, and H. W. Posamentier, 2011, Mass-transport deposits in deepwater settings, SEPM Soc for Sed Geology.

Sikkema, W., and K. M. Wojcik, 2000, 3D Visualization of Turbidite Systems, Lower Congo Basin, Offshore Angola, *in* P. Weimer, ed., Deep-Water Reservoirs of the World, SEPM Society for Sedimentary Geology.

Sincavage, R., P. Weimer, and R. Bouroullec, 2004, Sequence Stratigraphy of Upper-Miocene to Pleistocene Sediments of Southwestern Mississippi Canyon and Northwestern Atwater Valley, Northern Gulf of Mexico.

Sobiesiak, M. S., B. Kneller, G. I. Alsop, and J. P. Milana, 2016, Internal deformation and kinematic indicators within a tripartite mass transport deposit, NW Argentina: Sedimentary Geology.

Solheim, A., P. Bryn, H. Sejrup, J. Mienert, and K. Berg, 2005, Ormen Lange—an integrated study for the safe development of a deep-water gas field within the Storegga Slide Complex, NE Atlantic continental margin; executive summary, Ormen Lange–an Integrated Study for Safe Field Development in the Storegga Submarine Area, Elsevier, p. 1-9.

Strasser, M., P. Henry, T. Kanamatsu, M. K. Thu, G. F. Moore, and I. Expedition, 2012, Scientific drilling of mass-transport deposits in the Nankai accretionary wedge: First results from IODP Expedition 333, Submarine mass movements and their consequences, Springer, p. 671-681.

Strong, H. E., 2009, The origin and properties of mass transport deposits, Ursa Basin, Gulf of Mexico.

Talling, P. J., D. G. Masson, E. J. Sumner, and G. Malgesini, 2012, Subaqueous sediment density flows: Depositional processes and deposit types: Sedimentology, v. 59, p. 1937-2003.

Urgeles, R., and A. Camerlenghi, 2013, Submarine landslides of the Mediterranean Sea: Trigger mechanisms, dynamics, and frequency - magnitude distribution: Journal of Geophysical Research: Earth Surface, v. 118, p. 2600-2618.
Van Bemmel, P. P., and R. E. Pepper, 2000, Seismic signal processing method and apparatus for generating a cube of variance values, Google Patents.
Varnes, D. J., 1978, Slope movement types and processes: Special report, v. 176, p. 11-33.
Weimer, P., P. Varnai, F. M. Budhijanto, Z. M. Acosta, R. E. Martinez, A. F. Navarro, M. G. Rowan, B. C. McBride, T. Villamil, and C. Arango, 1998, Sequence stratigraphy of Pliocene and Pleistocene turbidite systems, northern Green Canyon and Ewing Bank (offshore Louisiana), northern Gulf of Mexico: AAPG bulletin, v. 82, p. 918-960.
Winker, C. D., and J. R. Booth, 2000, Sedimentary dynamics of the salt-dominated continental slope, Gulf of Mexico: integration of observations from the seafloor, near-surface, and deep subsurface: GCSSEPM Foundation 20th Annual Research Conference, Deep-Water Reservoirs of the World, p. 1059-1086.

Figure captions

Figure 1. Location map of the study area and study area relative to the globe map, showing the study area (red box), the position of the modern shelf edge (black dotted line), Pleistocene-shelf edge (white dotted line), and modern depositional systems. The location of the Pleistocene-shelf edge is inferred from Galloway et al. (2011), the Northern Gulf of Mexico Deepwater Bathymetry is created by using Arcgis, the hillshade map is cited from The Bureau of Ocean Energy Management (BOEM).

Figure 2. Seabed map along the study area and depth map for top salt (from 3D seismic data), showing the overall salt-tectonic structure of the study area. 1-5 and A-C refer to minibasins and salt structures, respectively, described in the text, and the contour interval is 500 m.

Figure 3. (A) N-S trending seismic section showing the overall salt-tectonic structure of the study area. (B) The eight key seismic horizons (H0 to seabed) and main MTC-bearing intervals. (C) The main seismic facies and depositional element interpretation, please note that colour in the legend refers to the different types of seismic facies. See Figure 2 for the location of the seismic line. Note the position of well AT-8 #1 ST.

Figure 4. (A) Variance attribute calculated for the interval between the H1 and H2 seismic horizons. The red dot indicates the well location; A-C are salt diapirs referred to in the text. (B) Sketch of MTC 1 indicating some of the key internal structures. Note: (i) the ramp; (ii) the MTC lateral margin; (iii) salt-related normal faults, (iv) intra-MTC thrusts; and (v) transported blocks. (C) WNW-ESE trending seismic profile showing the range of seismic facies within MTC 1 (see figure 4A for location). (D) ENE-WSW trending seismic profile showing the range of seismic facies within MTC 1. See figure 4A for location, the definition of the polarity and AI

convention in Figure 3A, and the un-interpreted seismic sections in supplementary material 4.

Figure 5. (A) Wireline logs, interpreted lithology, and extracted seismic reflection of MTC 1. Log tracks are gamma ray, sonic (DTCO1), resistivity (ATR1), lithology interpreted by gamma ray and acoustic log. (B) V_{shale} (Vsh) against P-wave velocity (Vp) cross plot for three seismic facies associations within MTC 1. Each seismic facies tend to plot in a distinct cluster with however some dots are plotting away from correlated cluster. Note in Fig. 5A the black dashed lines are top and base boundaries of MTC1, and the black dotted lines are boundaries of each seismic facies. DTCO stands for Delta-Time Compressional (microsec/ft), ATR stands for Attenuation resistivity (deep; ohm-m). The depth is in measured depth.

Figure 6. (A) Variance attribute calculated on the H2.1 seismic horizon. The red dot indicates the well location; A-C are salt diapirs referred to in the text. (B) Sketch of MTC 2 indicating some key structures and features. Note: (i) the remnant block, (ii) salt-related normal faults, and (iii) lateral margin. (C) NNE-SSW trending seismic profile showing the range of seismic facies within MTC 2 (see figure 4.1 for location). (D) WWE-ESE trending seismic profile showing the range of seismic facies within MTC 2 (see figure 6A for location). The vertical axis is in measured depth. See figure 6A for location, the definition of the polarity and AI convention in Figure 3A, and the un-interpreted seismic sections in supplementary material 5.

Figure 7. (A) Wireline logs, interpreted lithology, and extracted seismic reflection of MTC 2. Log tracks are gamma ray, sonic (DTCO1), resistivity (ATR1), lithology interpreted by gamma ray and acoustic log. (B) V_{shale} (Vsh) against P-wave velocity (Vp) cross plot for three seismic facies associations within MTC 2. Each seismic facies tend to plot in a distinct cluster with

however some dots are plotting away from correlated cluster. Note in Fig. 7A the black dashed lines are top and base boundaries of MTC2, and the black dotted lines are boundaries of each seismic facies. DTCO stands for Delta-Time Compressional (microsec/ft), ATR stands for Attenuation resistivity (deep; ohm-m). The depth is in measured depth.

Figure 8. (A) Chaos attribute calculated for the interval between the H4 and H4.1 seismic horizons. The red dot indicates the well location; A-C are salt diapirs referred to in the text. (B) Sketch of MTC 3 indicating some key structures and features. Note: (i) the remnant block, (ii) salt-related normal faults, and (iii) lateral margin. (C) WWE-trending seismic profile showing the range of seismic facies within MTC 3 (see figure 8A for location). (D) WWE-trending seismic profile showing the range of seismic facies within MTC 3. See figure 8A for location, the definition of the polarity and AI convention in Figure 3A, and the un-interpreted seismic sections in supplementary material 6.

Figure 9. (A) Wireline logs and interpreted lithology of MTC 3. Log tracks are gamma ray, acoustic (DTCO1), resistivity (ATR1), lithology interpreted by gamma ray and acoustic log, and extracted seismic reflection. Note the black dashed lines are top and bottom boundaries of MTC1, black dotted lines are boundaries of each seismic facies. DTCO stands for Delta-Time Compressional (microsec/ft), ATR stands for Attenuation resistivity (deep; ohm-m). (B) V_{shale} against Velocity cross plot for seismic facies 3.2 associations within MTC 3. The depth is in measured depth.

Figure 10. (A) P-wave velocity (Vp) log, interpreted lithology column, and a schematic sketch of Vp depth trend. (B) Resistivity (Rt) log, interpreted lithology column and correlated seismic section. Note that the dotted black line in Figure 10A indicates inferred hydrostatic trend based on Vp log.

Figure 11. (A) Amplitude map extracted at the top surface of MTC 1 and its correlative surface overlying undeformed strata. Yellowish colour occurs when MTC 1 underlies the surface, and blueish colour corresponds to the surface overlying undeformed strata. (B) Amplitude map extracted at basal shear surface of MTC 1 and its correlative surface underlying undeformed strata. Bright amplitude occurs when MTC 1 overlays the surface, and dim amplitude corresponds to the surface underlying undeformed strata. (C) Schematic cross-section of MTC 1 and its correlative undeformed strata, see location from Figure 11A.

Figure 12. (A) Velocity (Vp) and Resistivity (Rt) logs of mudstone-rich deposits covering background and MTC deposits. (B) Velocity (Vp) and Resistivity (Rt) logs of sandstone-rich deposits covering background and MTC deposits, and their correlated seismic section.

Figure 13. (A) Velocity (Vp) and Resistivity (Rt) logs of MTC 3. (B) Velocity (Vp) and Resistivity (Rt) logs of MTC 2. (C) Velocity (Vp) and Resistivity (Rt) logs of MTC 1, see the depth interval from Velocity (Vp) log in Figure 10.

Figure 14 a) Schematic sketch of MTC and its basal shear zone; b) schematic sketch of Vp and RT logs within MTC intervals. Schematic sketch of processes within the basal shear zone (see location in a): liquefaction (c); fluid escape (d); overcompaction (e).

Table captions

Table 1 Summary of seismic facies in minibasin 5, including well logs, lithology, schematic facies geometries, facies characteristics, and depositional environment.

Table 2 Approximate dimensions of MTCs by log mapping. Note that the thickness of MTCs indicate the maximum total thickness.

Figure 1

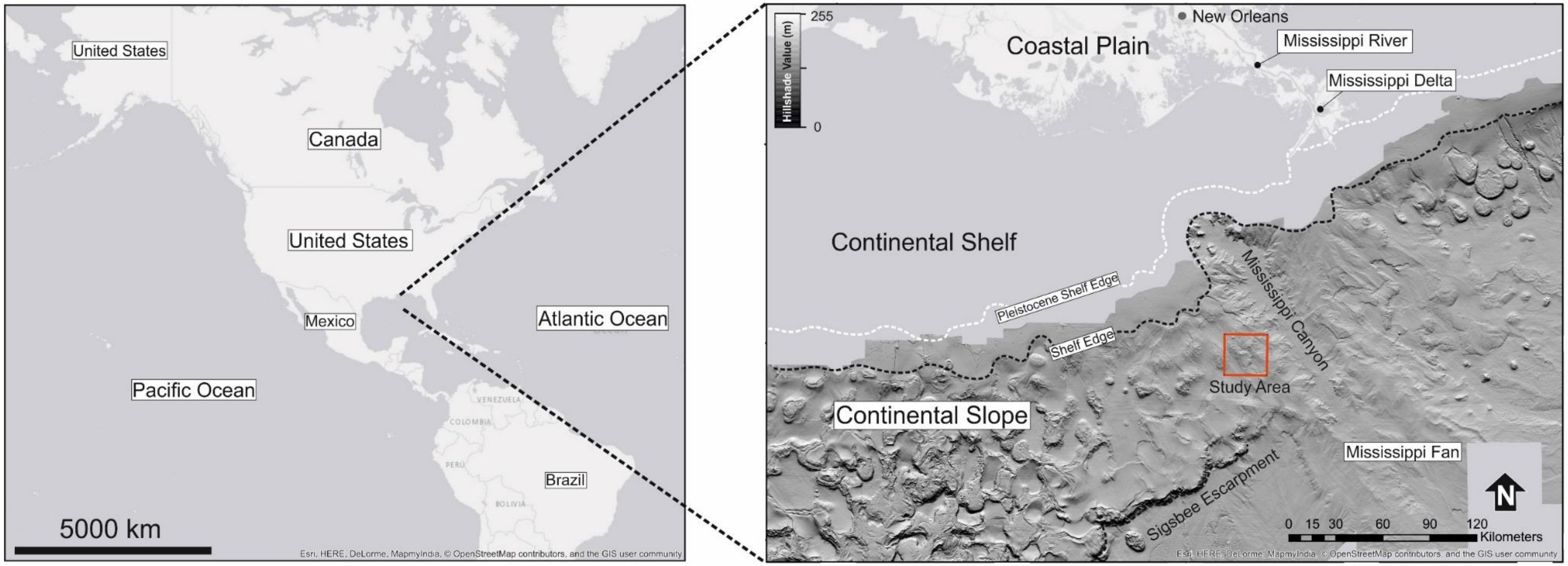

United States
Canada
United States
Mexico
Atlantic Ocean
Pacific Ocean
Brazil
5000 km
Esri, HERE, DeLorme, MapmyIndia, © OpenStreetMap contributors, and the GIS user community
255
Hillshade Value (m)
0
New Orleans
Coastal Plain
Mississippi River
Mississippi Delta
Continental Shelf
Pleistocene Shelf Edge
Shelf Edge
Mississippi Canyon
Study Area
Continental Slope
Sigsbee Escarpment
Mississippi Fan
N
0 15 30 60 90 120
Kilometers
Esri, HERE, DeLorme, MapmyIndia, © OpenStreetMap contributors, and the GIS user community

Figure 2A

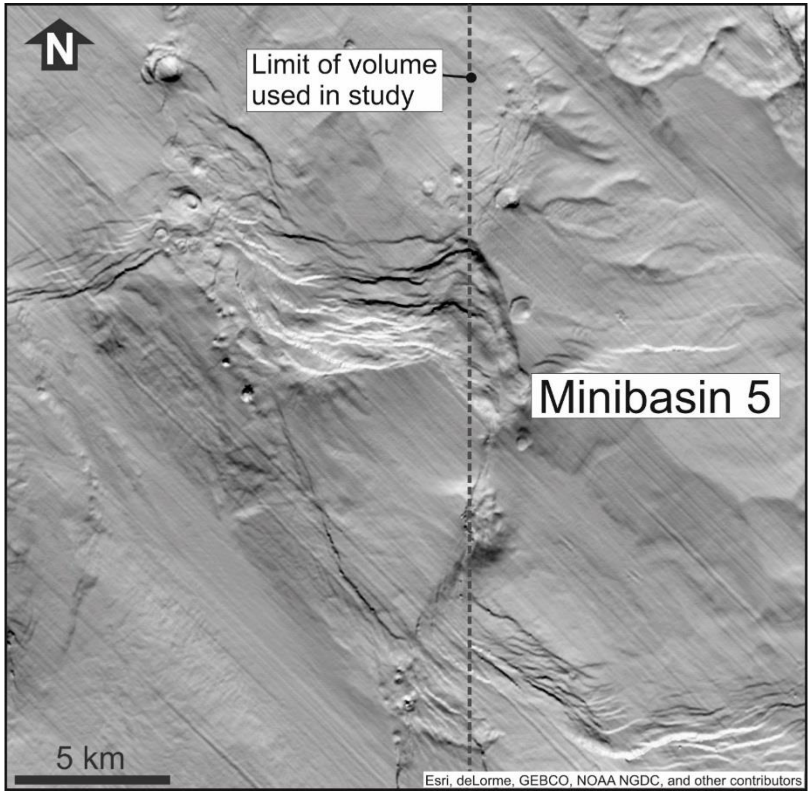

Figure 2B

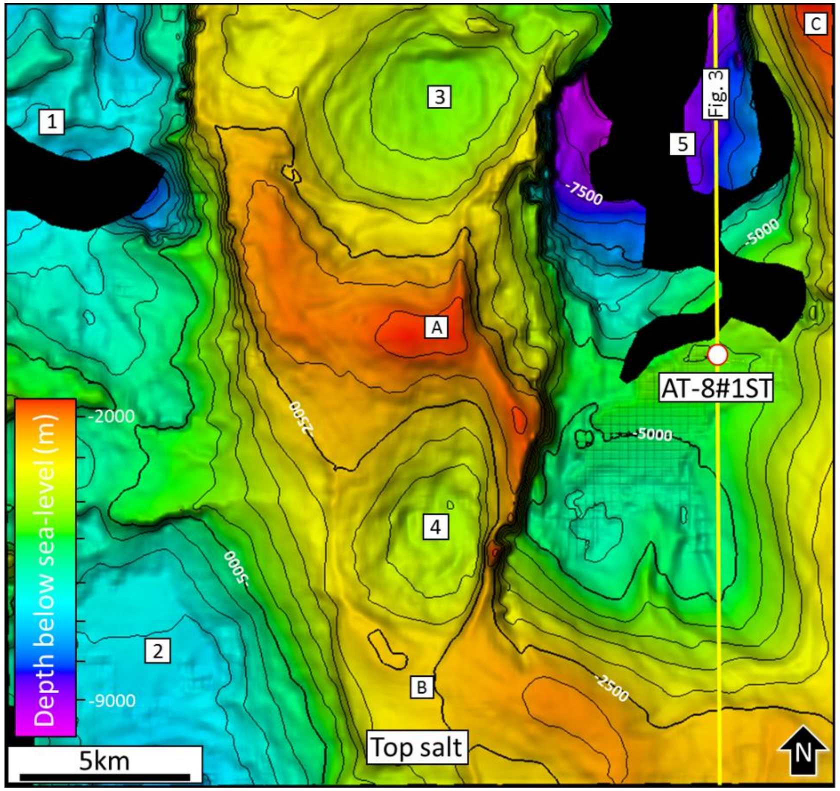

Figure 3A

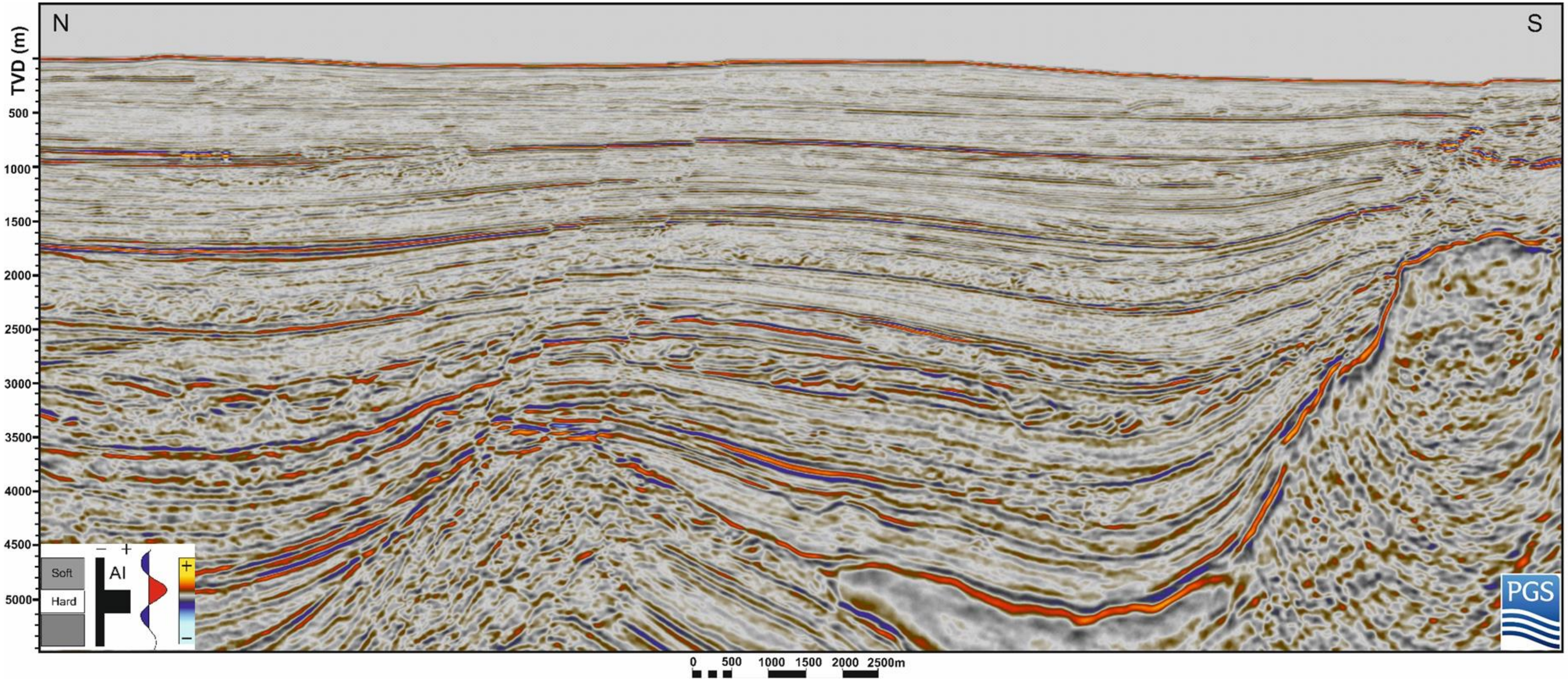
N
S
TVD (m)
500
1000
1500
2000
2500
3000
3500
4000
4500
5000
Soft
Hard
AI
PGS
0
500
1000
1500
2000
2500m

Figure 3B

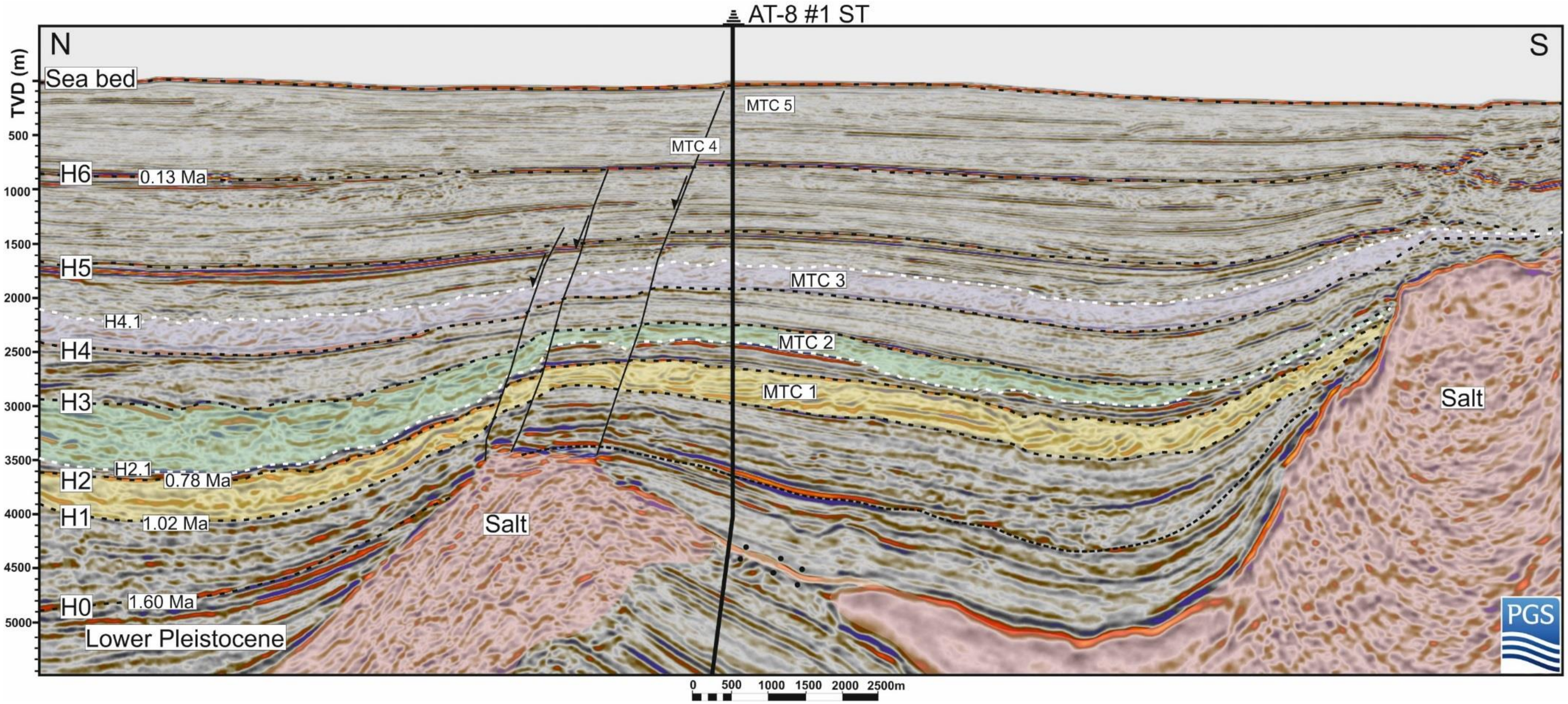
AT-8 #1 ST
N
S
TVD (m)
Sea bed
500
1000
1500
2000
2500
3000
3500
4000
4500
5000
H6
0.13 Ma
H5
H4.1
H4
H3
H2.1
H2
0.78 Ma
H1
1.02 Ma
H0
1.60 Ma
Lower Pleistocene
MTC 5
MTC 4
MTC 3
MTC 2
MTC 1
Salt
Salt
PGS
0 500 1000 1500 2000 2500m

Figure 3C

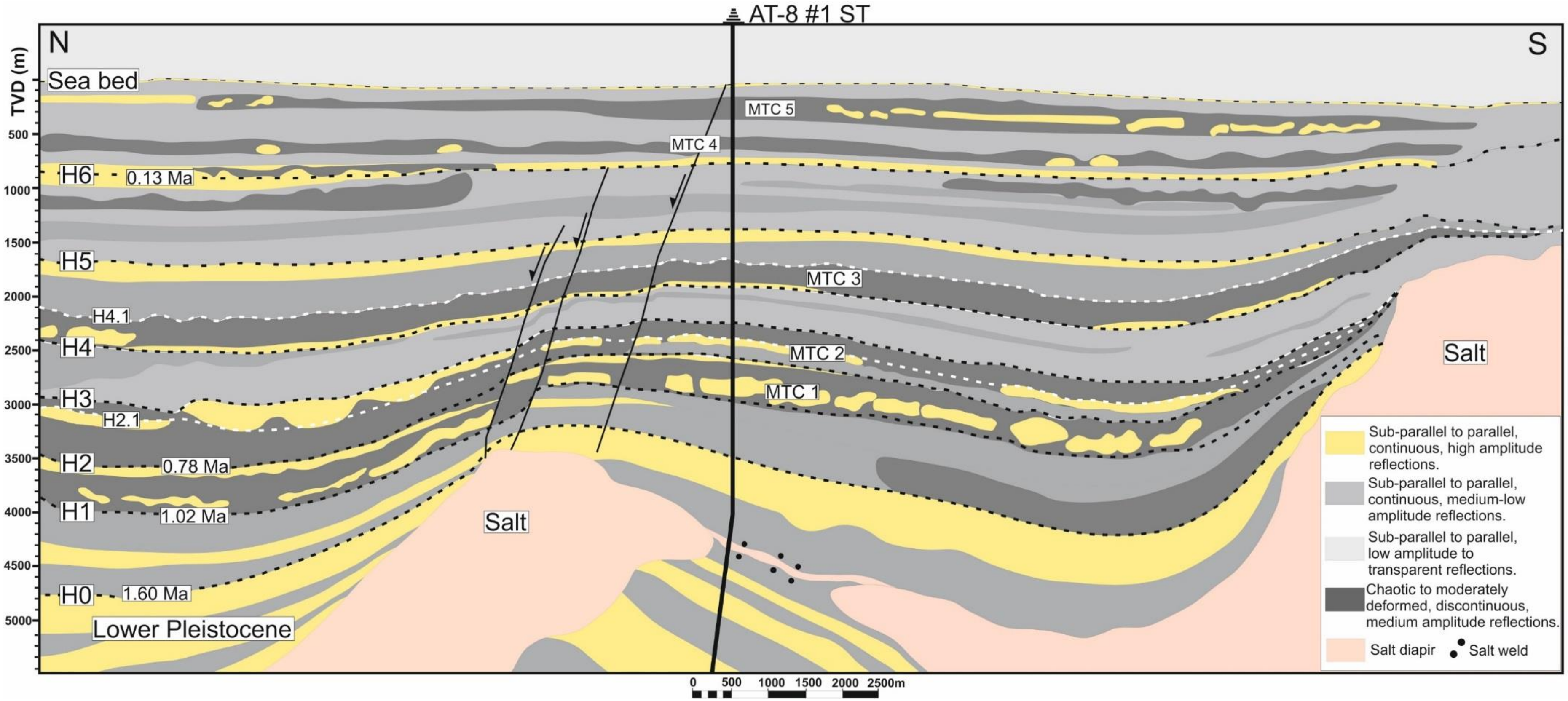

AT-8 #1 ST
N
S
TVD (m)
Sea bed
500
1000
1500
2000
2500
3000
3500
4000
4500
5000
MTC 5
MTC 4
H6
0.13 Ma
H5
MTC 3
H4.1
H4
MTC 2
H3
MTC 1
H2.1
H2
0.78 Ma
H1
1.02 Ma
H0
1.60 Ma
Lower Pleistocene
Salt
Salt
Sub-parallel to parallel, continuous, high amplitude reflections.
Sub-parallel to parallel, continuous, medium-low amplitude reflections.
Sub-parallel to parallel, low amplitude to transparent reflections.
Chaotic to moderately deformed, discontinuous, medium amplitude reflections.
Salt diapir
Salt weld
0 500 1000 1500 2000 2500m

Figure 4A

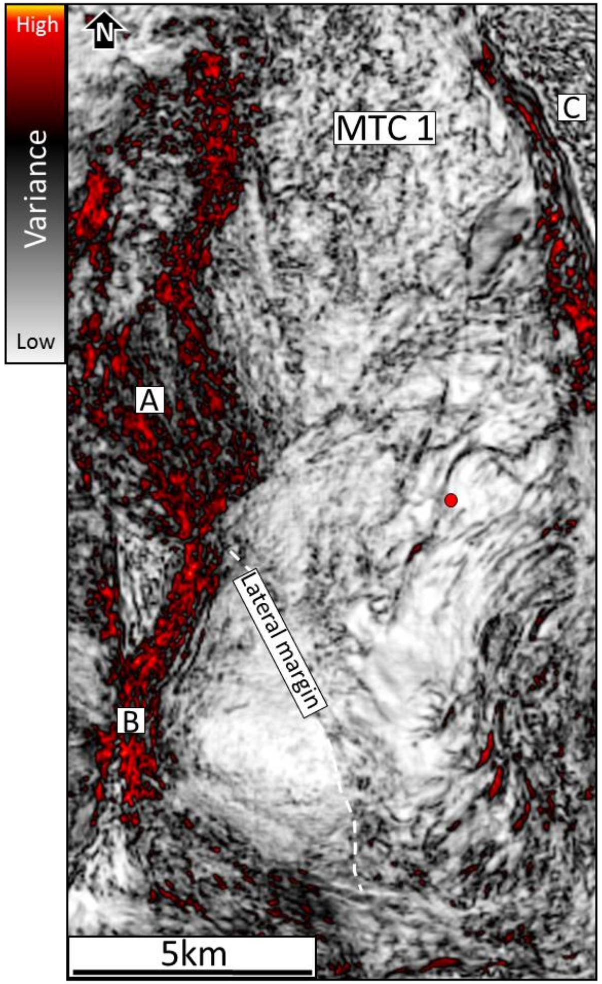

Figure 4B

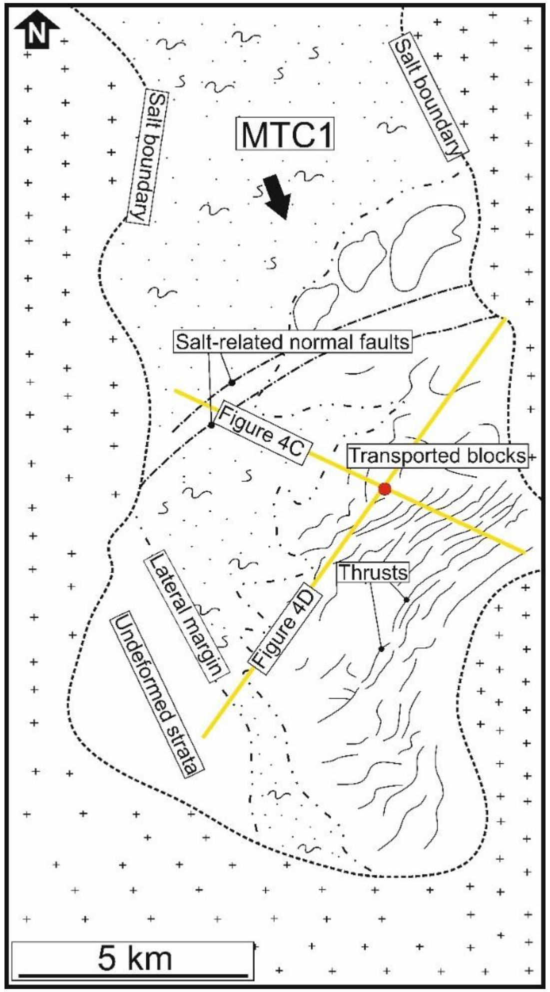

Figure 4C

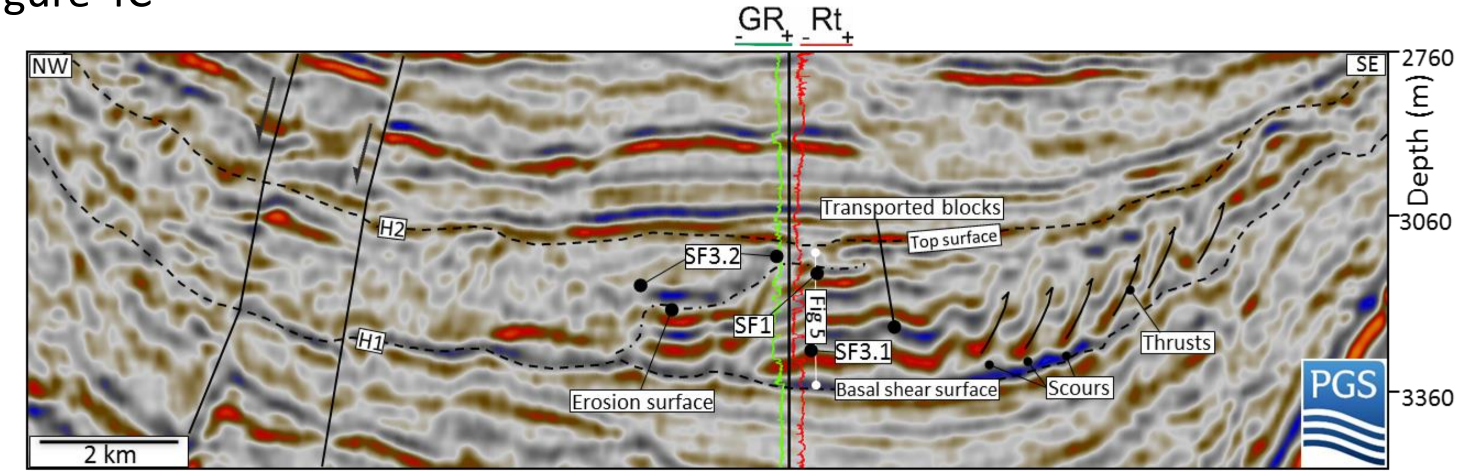

Figure 4D

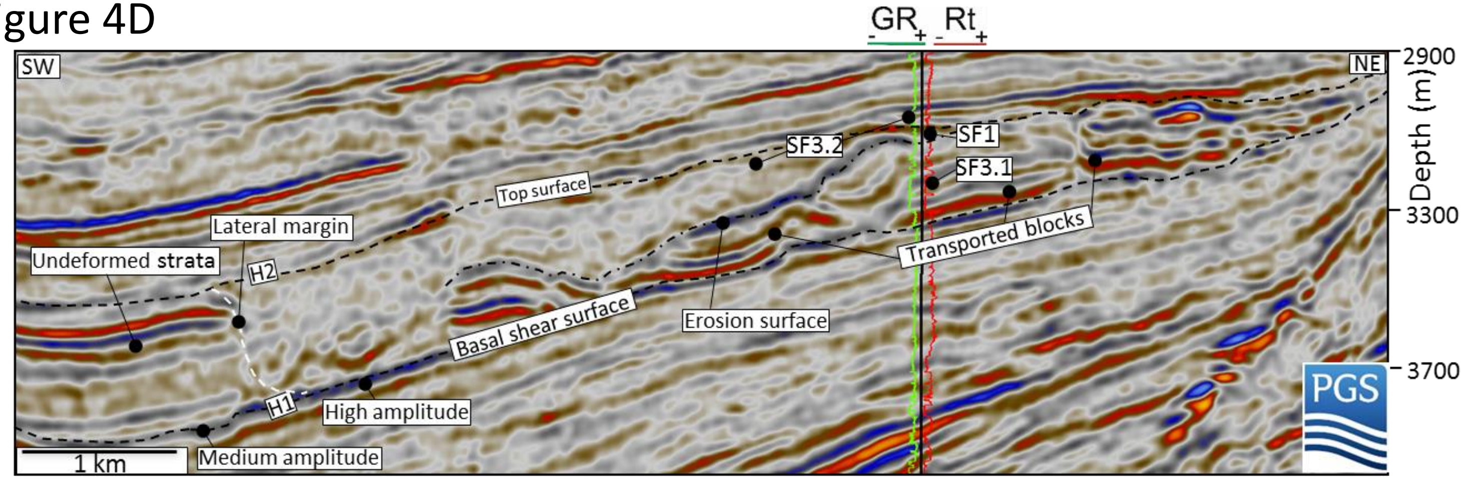

Figure 5A

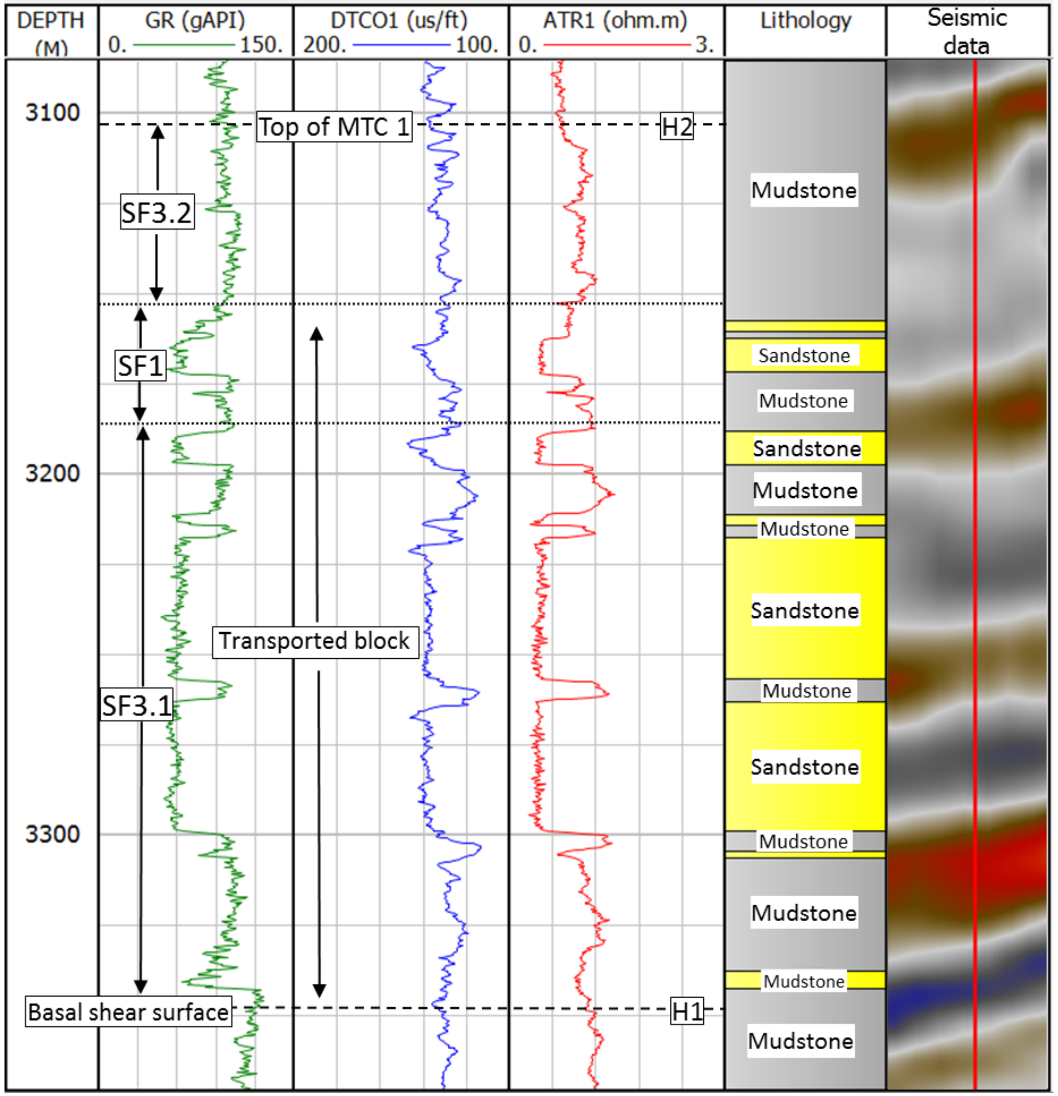

DEPTH (M)
GR (gAPI) 0. 150.
DTCO1 (us/ft) 200. 100.
ATR1 (ohm.m) 0. 3.
Lithology
Seismic data
3100
3200
3300
Top of MTC 1
H2
SF3.2
SF1
SF3.1
Transported block
Basal shear surface
H1
Mudstone
Sandstone
Mudstone
Sandstone
Mudstone
Mudstone
Sandstone
Mudstone
Sandstone
Mudstone
Mudstone
Mudstone
Mudstone

Figure 5B

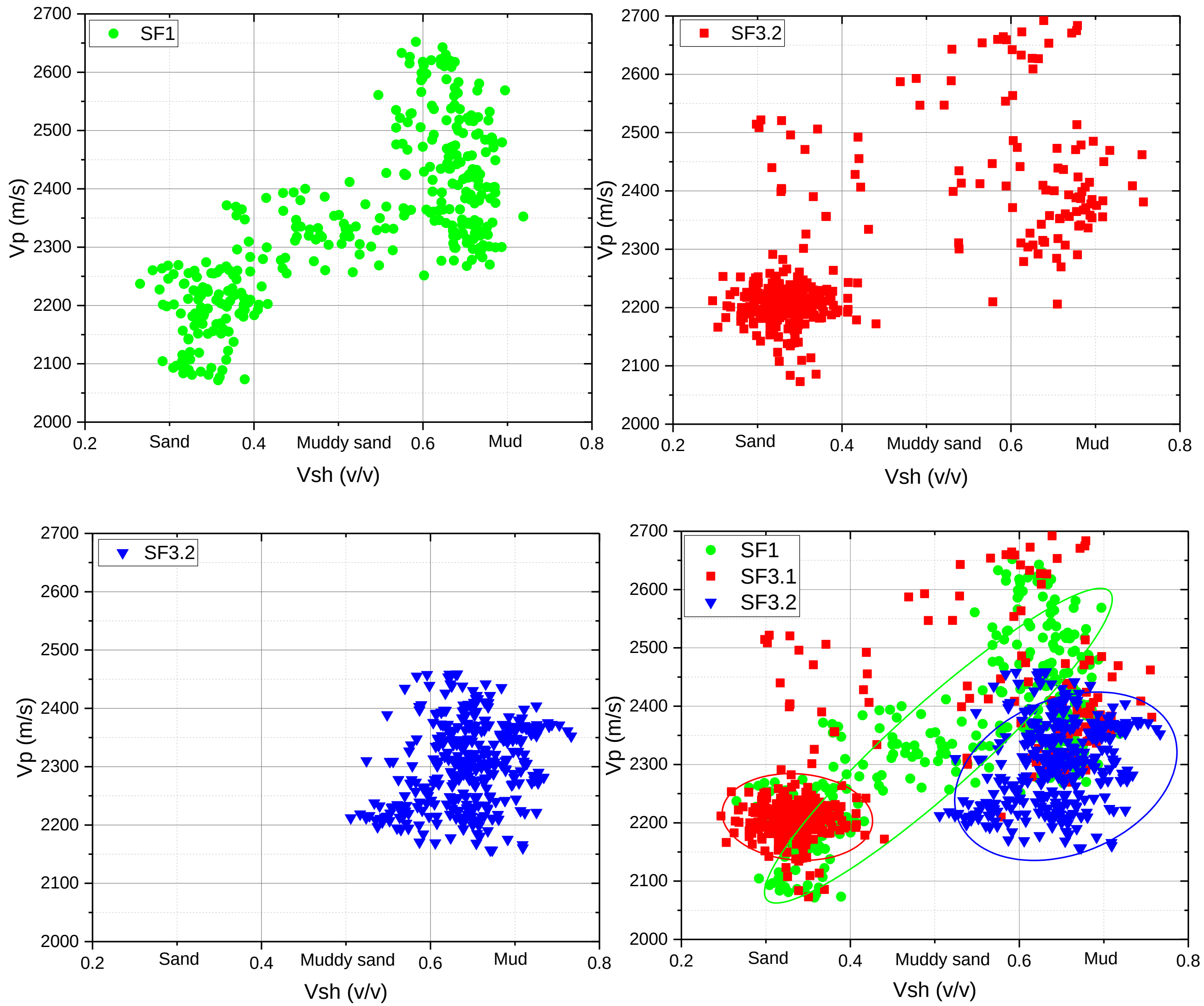
SF1
SF3.2
SF3.2
SF1
SF3.1
SF3.2
Vp (m/s)
Vsh (v/v)
2700
2600
2500
2400
2300
2200
2100
2000
0.2
Sand
0.4
Muddy sand
0.6
Mud
0.8

Figure 6A

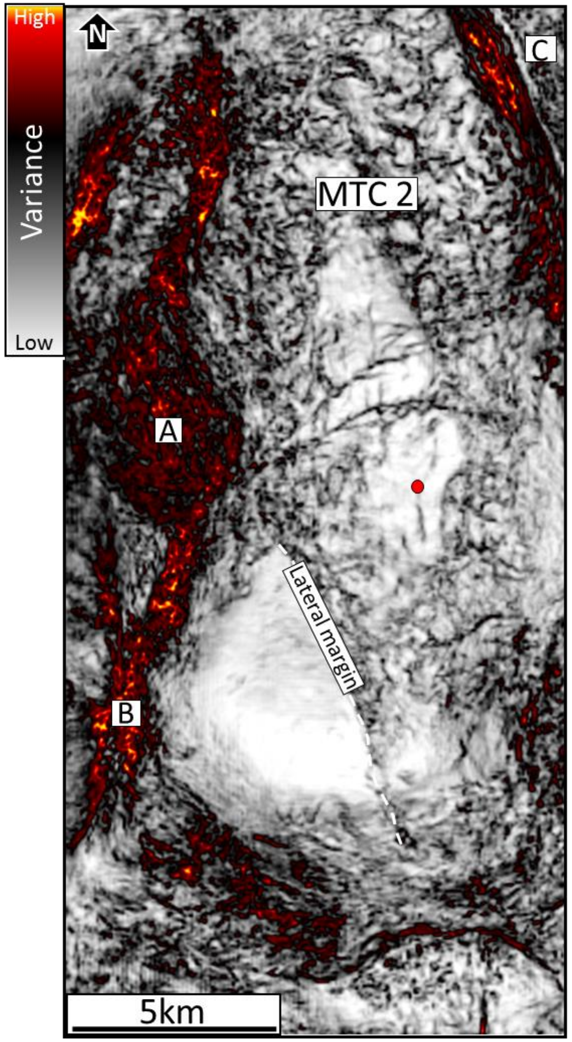

Figure 6B

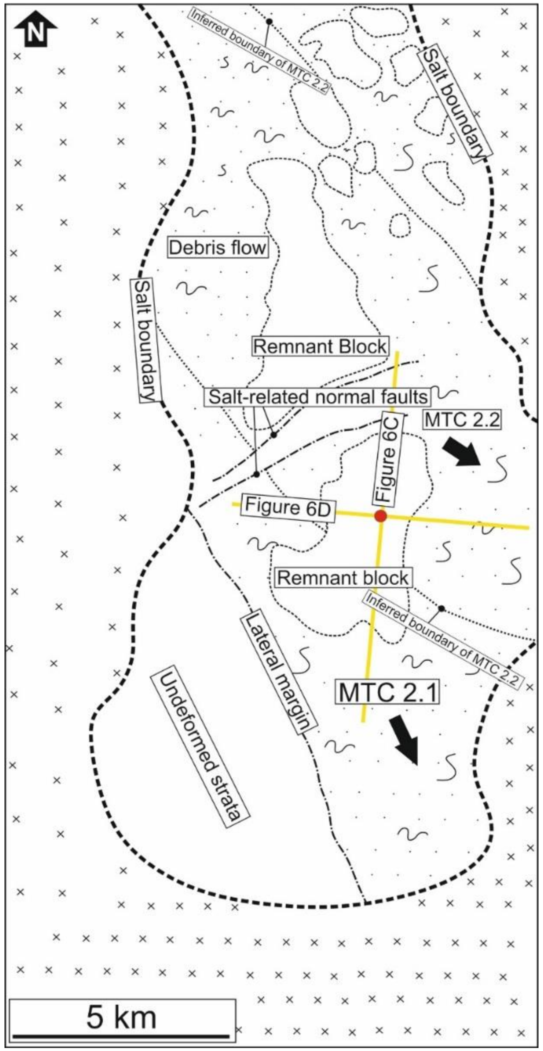

Figure 6C

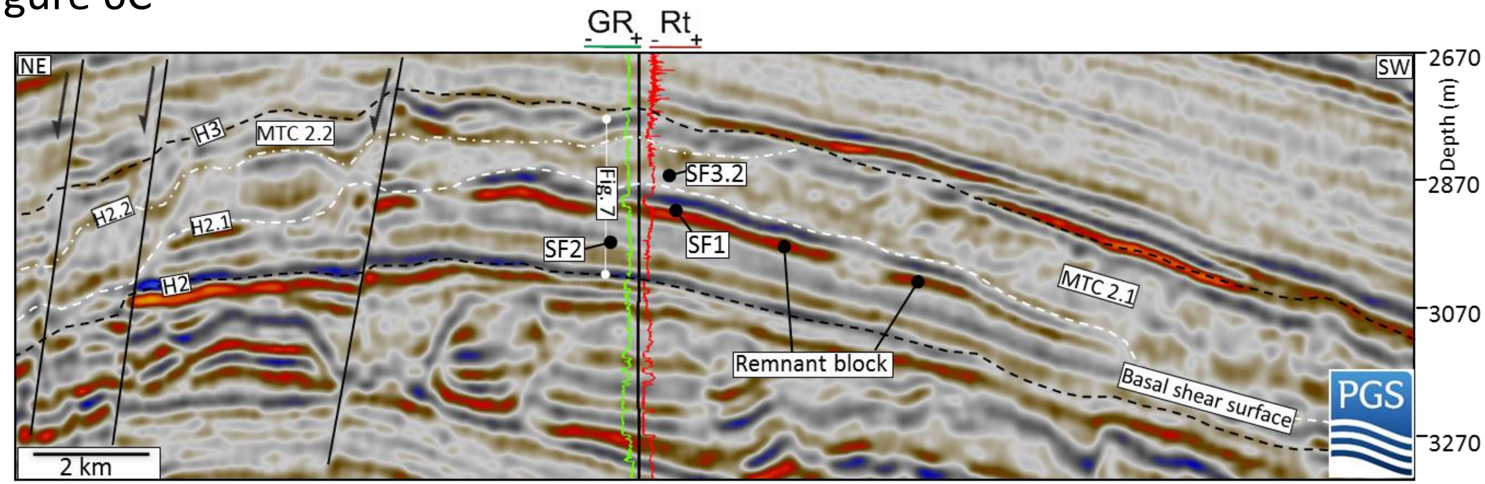

Figure 6D

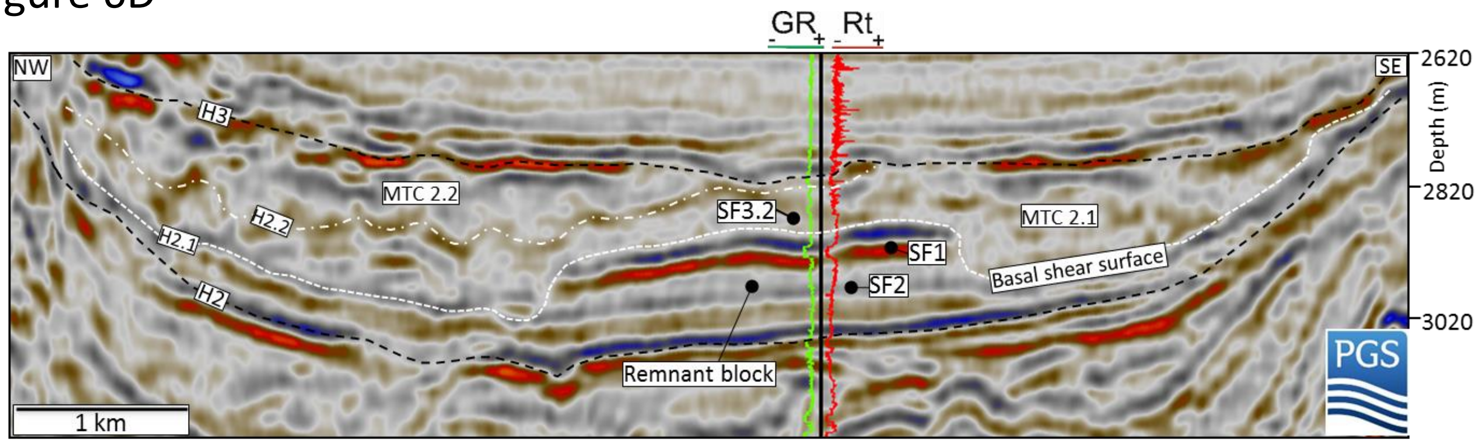

Figure 7A

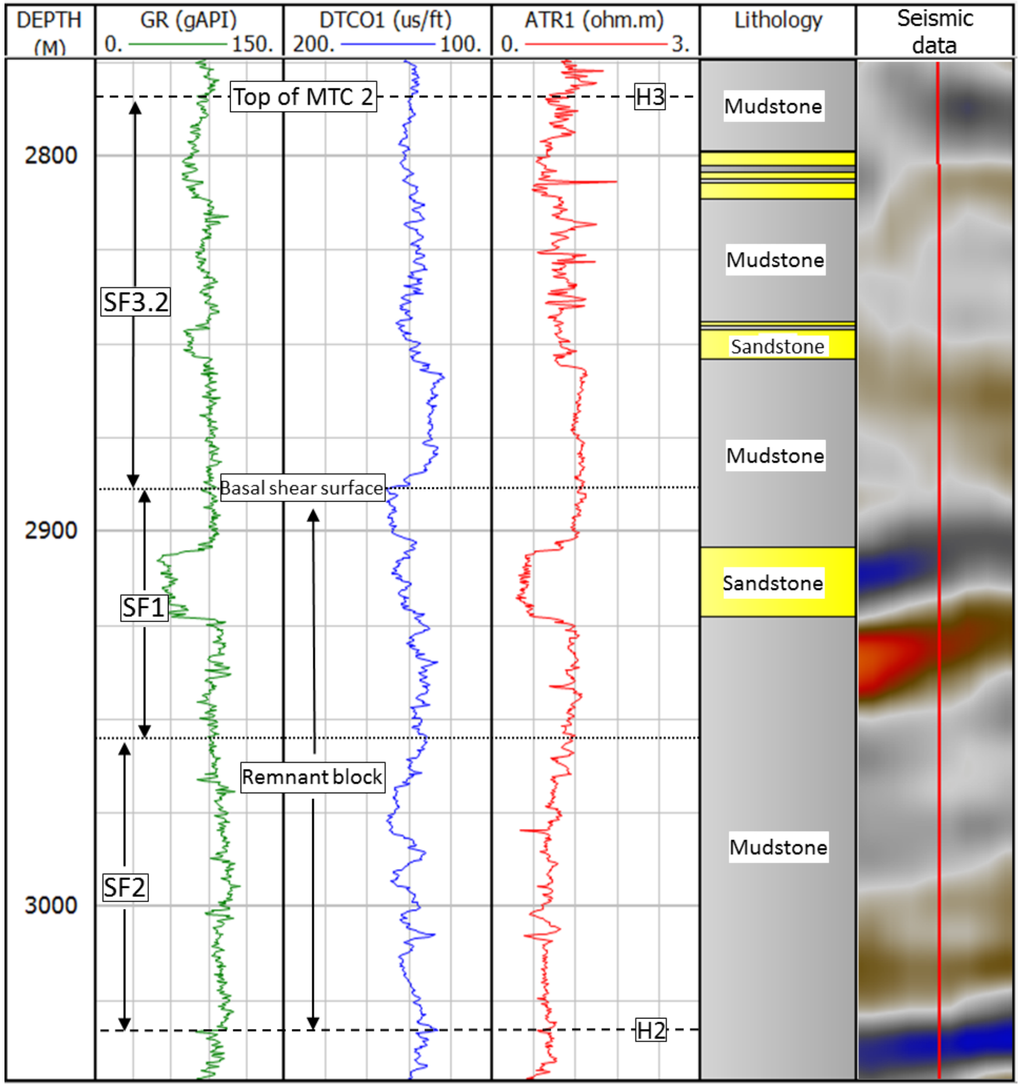

DEPTH (M)
GR (gAPI)
0.
150.
DTCO1 (us/ft)
200.
100.
ATR1 (ohm.m)
0.
3.
Lithology
Seismic data
2800
2900
3000
Top of MTC 2
H3
SF3.2
Basal shear surface
SF1
Remnant block
SF2
H2
Mudstone
Mudstone
Sandstone
Mudstone
Sandstone
Mudstone

Figure 7B

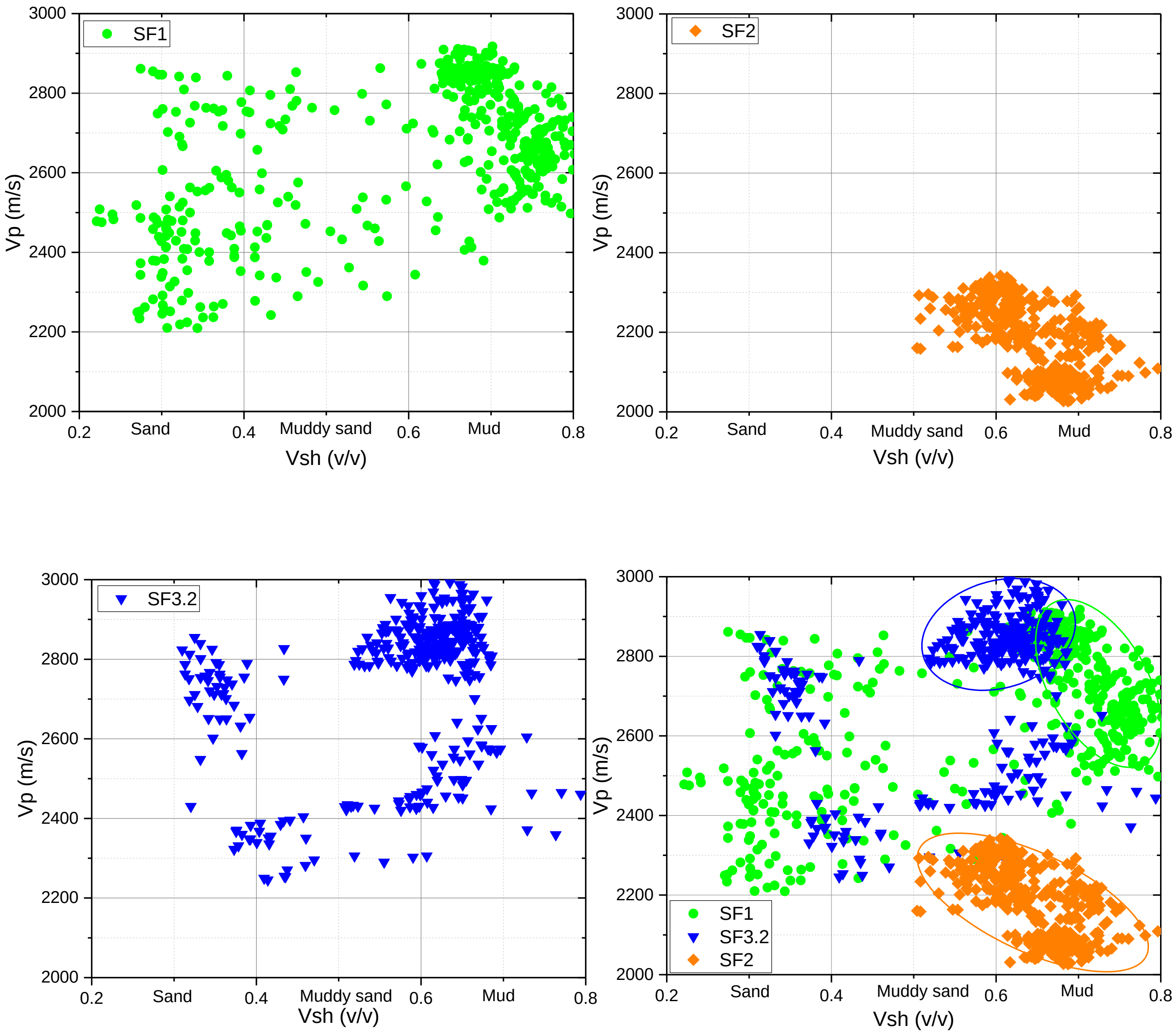
SF1
SF2
SF3.2
SF1
SF3.2
SF2
Vp (m/s)
Vsh (v/v)
Sand
Muddy sand
Mud
3000
2800
2600
2400
2200
2000
0.2
0.4
0.6
0.8

Figure 8A

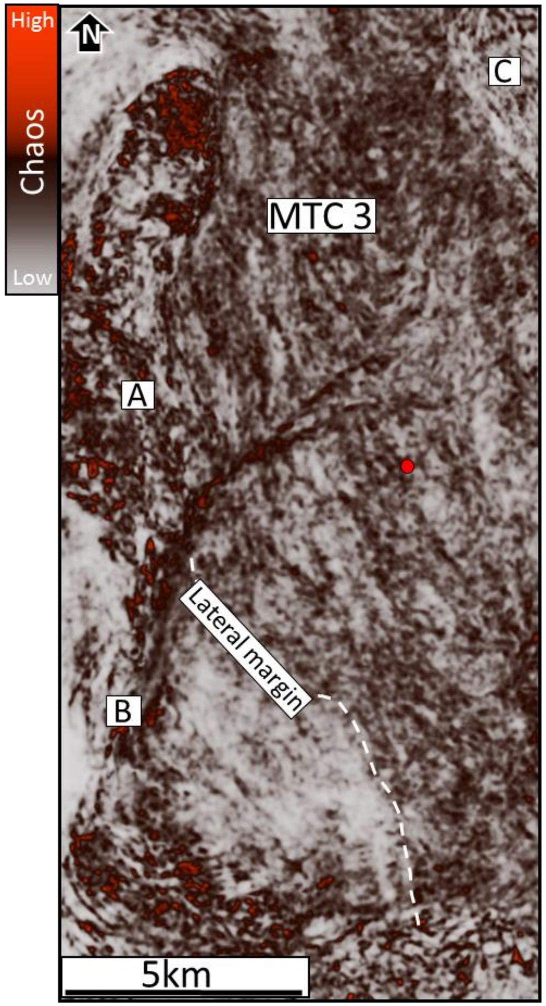

Figure 8B

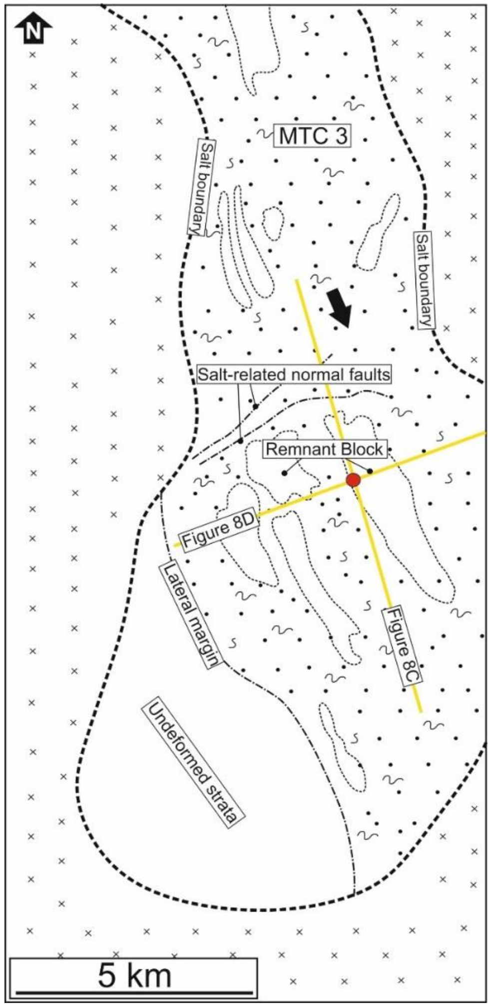

Figure 8C

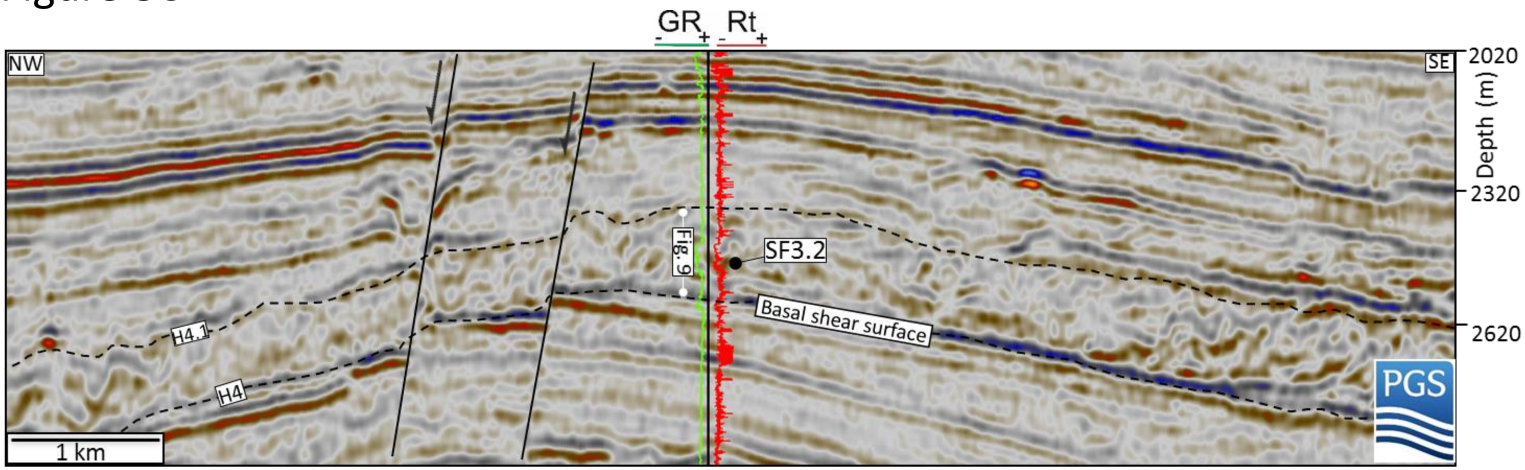

Figure 8D

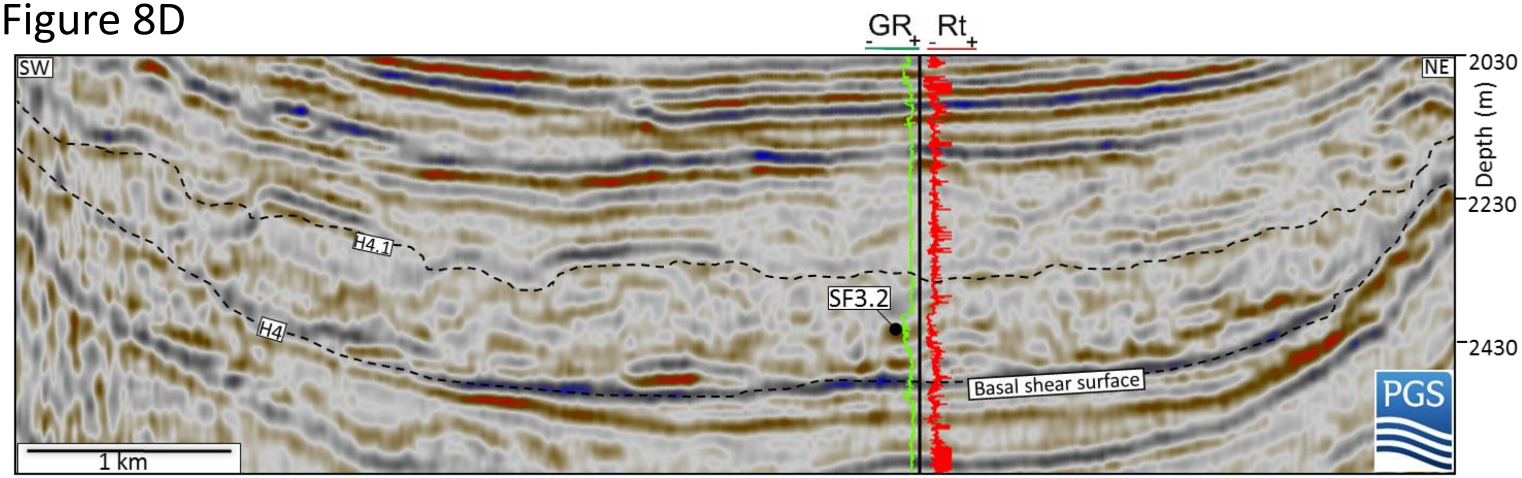

Figure 9A

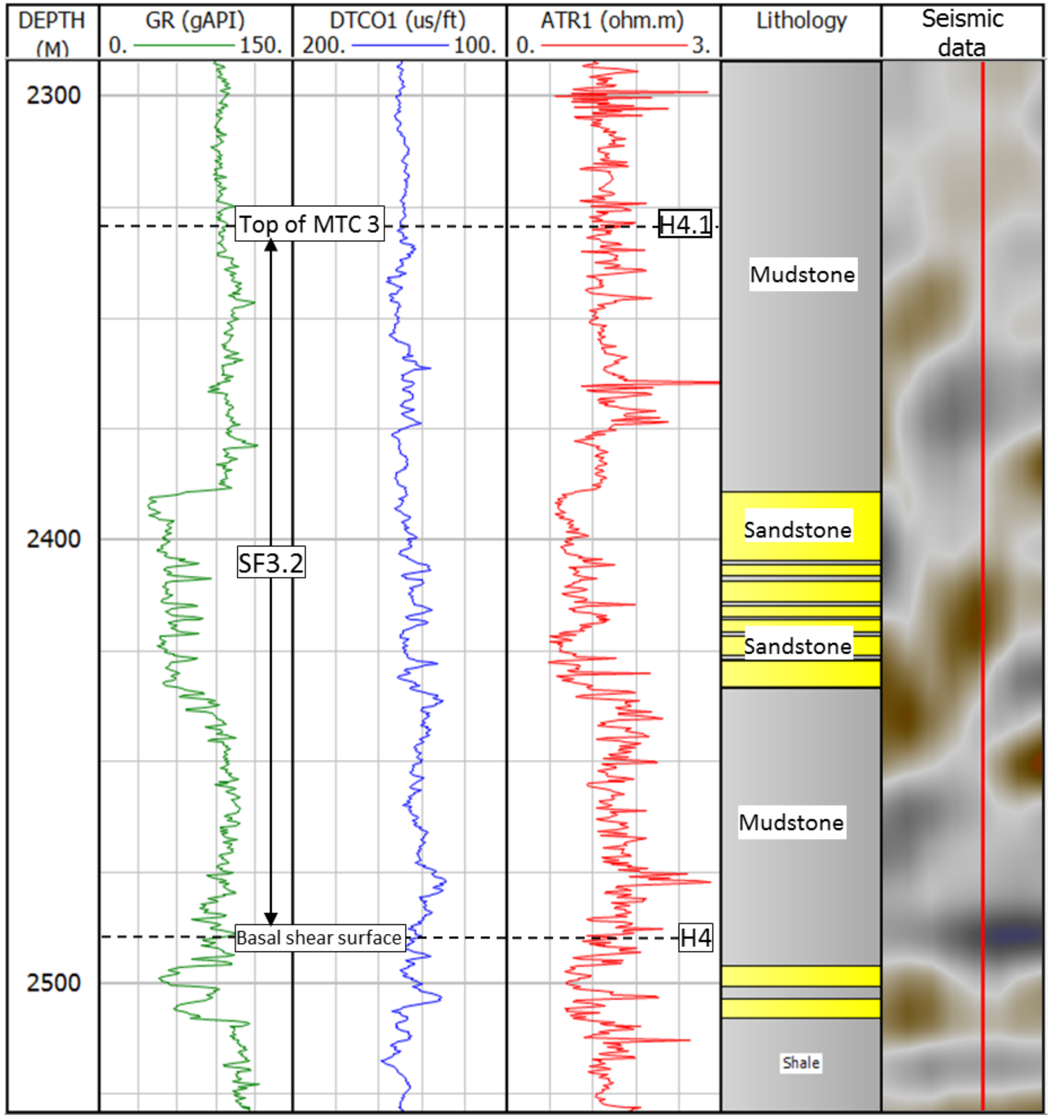

DEPTH (M)
GR (gAPI)
0.
150.
DTCO1 (us/ft)
200.
100.
ATR1 (ohm.m)
0.
3.
Lithology
Seismic data
2300
2400
2500
Top of MTC 3
H4.1
SF3.2
Basal shear surface
H4
Mudstone
Sandstone
Sandstone
Mudstone
Shale

Figure 9B

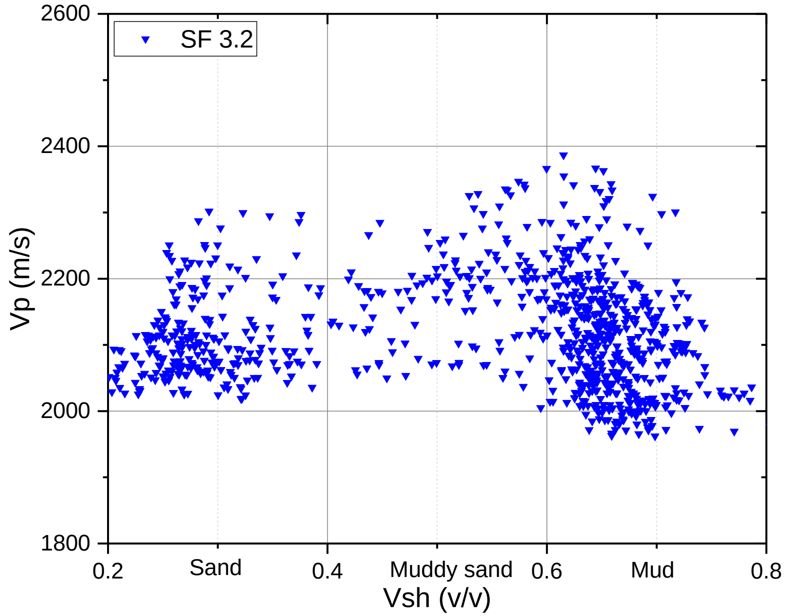

SF 3.2
2600
2400
2200
2000
1800
Vp (m/s)
0.2
Sand
0.4
Muddy sand
0.6
Mud
0.8
Vsh (v/v)

Figure 10A

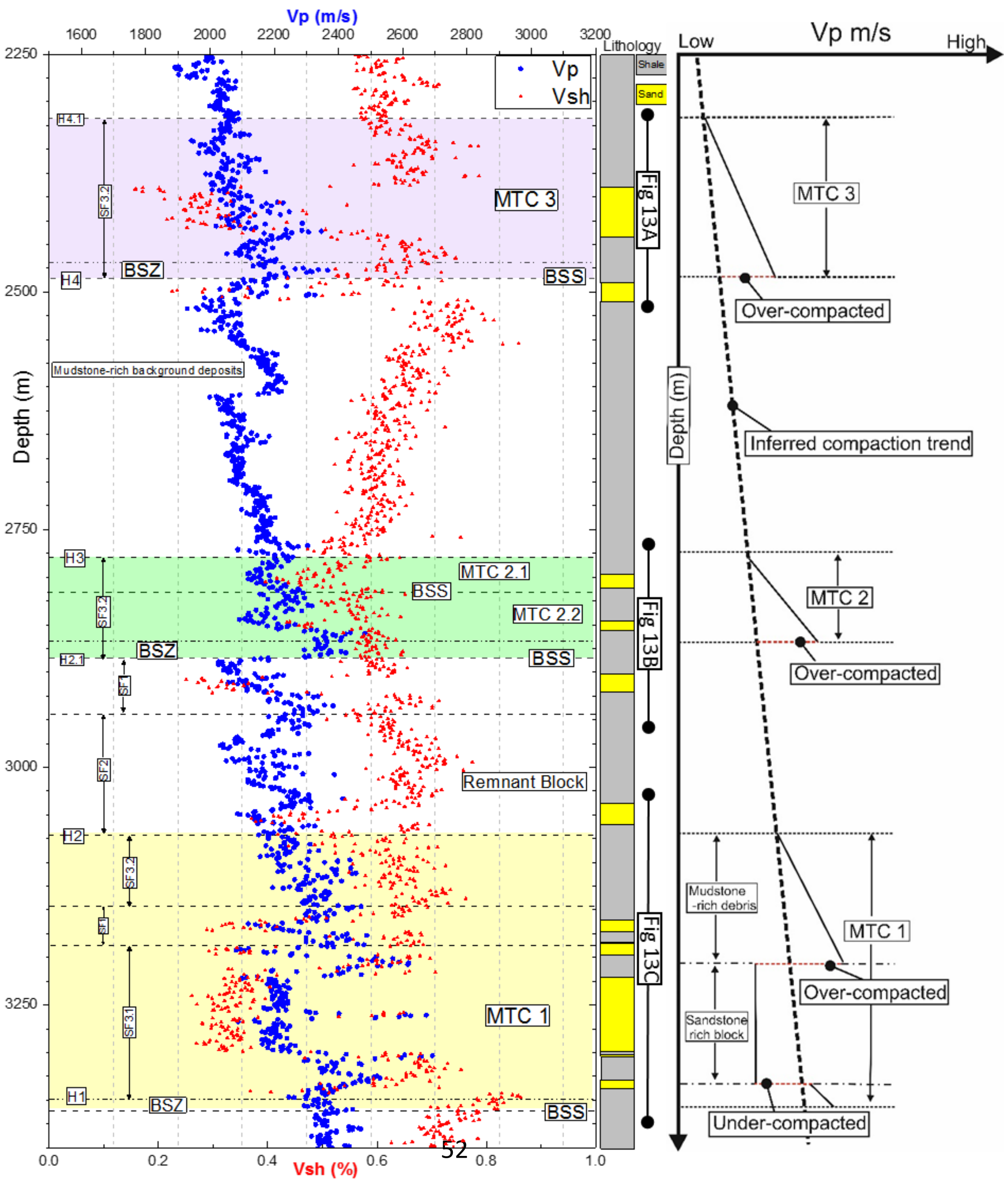

Vp (m/s)
Vp
Vsh
Depth (m)
Vsh (%)
Lithology
Shale
Sand
H4.1
H4
H3
H2.1
H2
H1
MTC 3
MTC 2.1
MTC 2.2
MTC 1
BSZ
BSS
Mudstone-rich background deposits
Remnant Block
Fig 13A
Fig 13B
Fig 13C
Vp m/s
Low
High
Depth (m)
Over-compacted
Inferred compaction trend
MTC 2
Mudstone -rich debris
Sandstone rich block
Under-compacted

Figure 10B

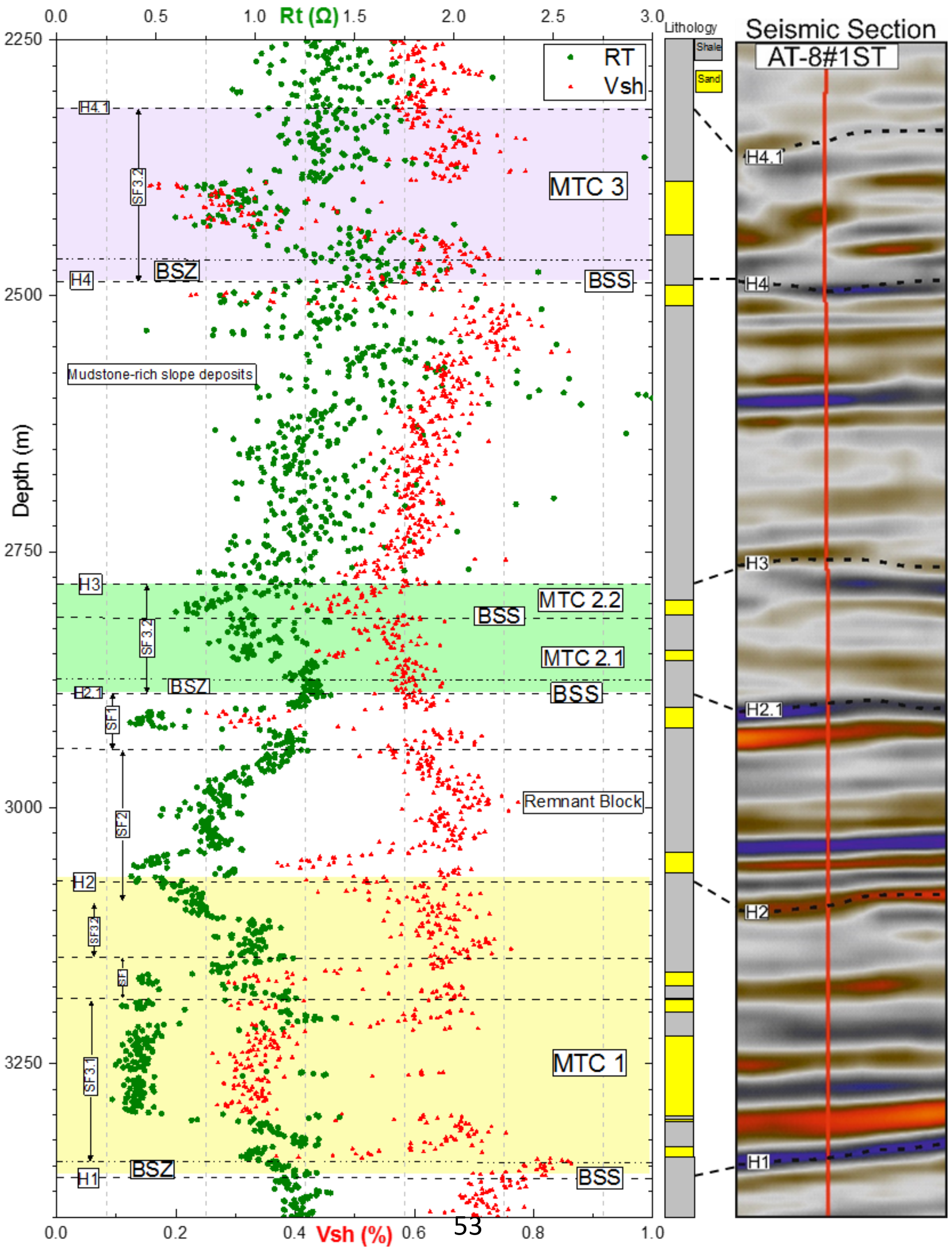

Rt (Ω)
0.0
0.5
1.0
1.5
2.0
2.5
3.0
RT
Vsh
Depth (m)
2250
2500
2750
3000
3250
H4.1
SF3.2
MTC 3
BSZ
H4
BSS
Mudstone-rich slope deposits
H3
MTC 2.2
BSS
MTC 2.1
BSZ
H2.1
BSS
SF1
SF2
Remnant Block
H2
SF3.2
SF3.1
MTC 1
BSZ
H1
BSS
0.0
0.2
0.4
Vsh (%)
0.6
0.8
1.0
Lithology
Shale
Sand
Seismic Section
AT-8#1ST
H4.1
H4
H3
H2.1
H2
H1

Figure 11A

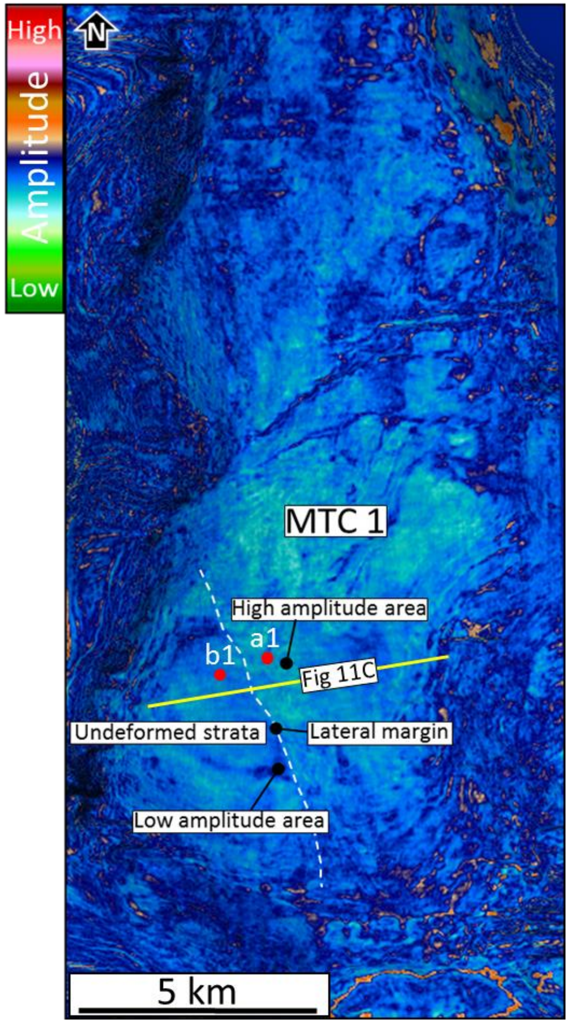

Figure 11B

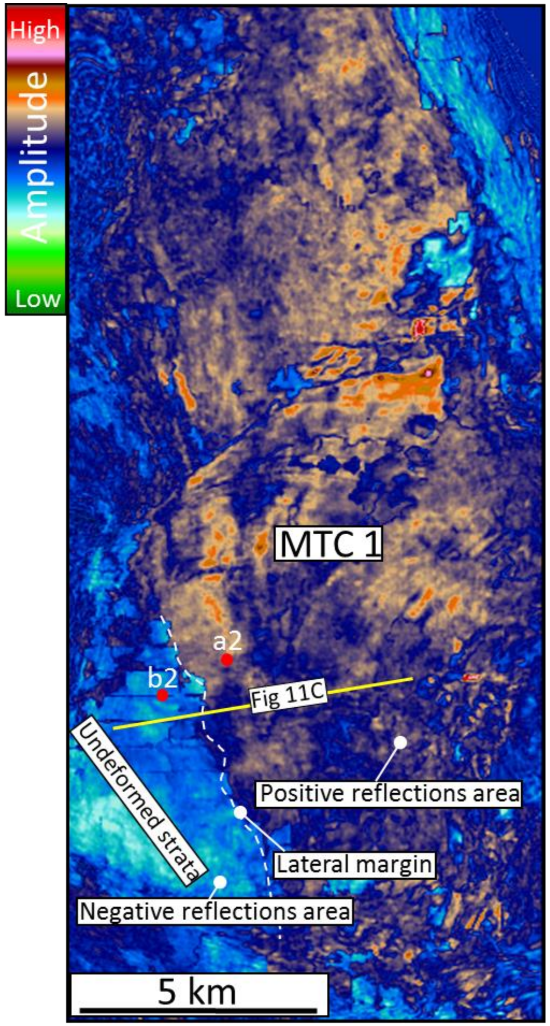

Figure 11C

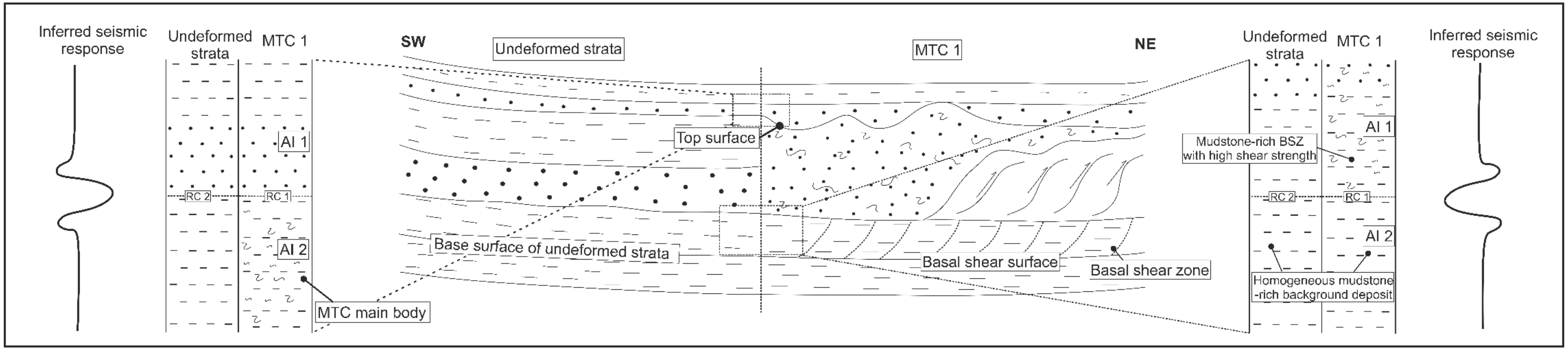

Inferred seismic response
Undeformed strata
MTC 1
AI 1
RC 2
RC 1
AI 2
MTC main body
SW
Undeformed strata
MTC 1
NE
Top surface
Base surface of undeformed strata
Basal shear surface
Basal shear zone
Undeformed strata
MTC 1
Inferred seismic response
AI 1
Mudstone-rich BSZ with high shear strength
RC 2
RC 1
AI 2
Homogeneous mudstone -rich background deposit

Figure 12A

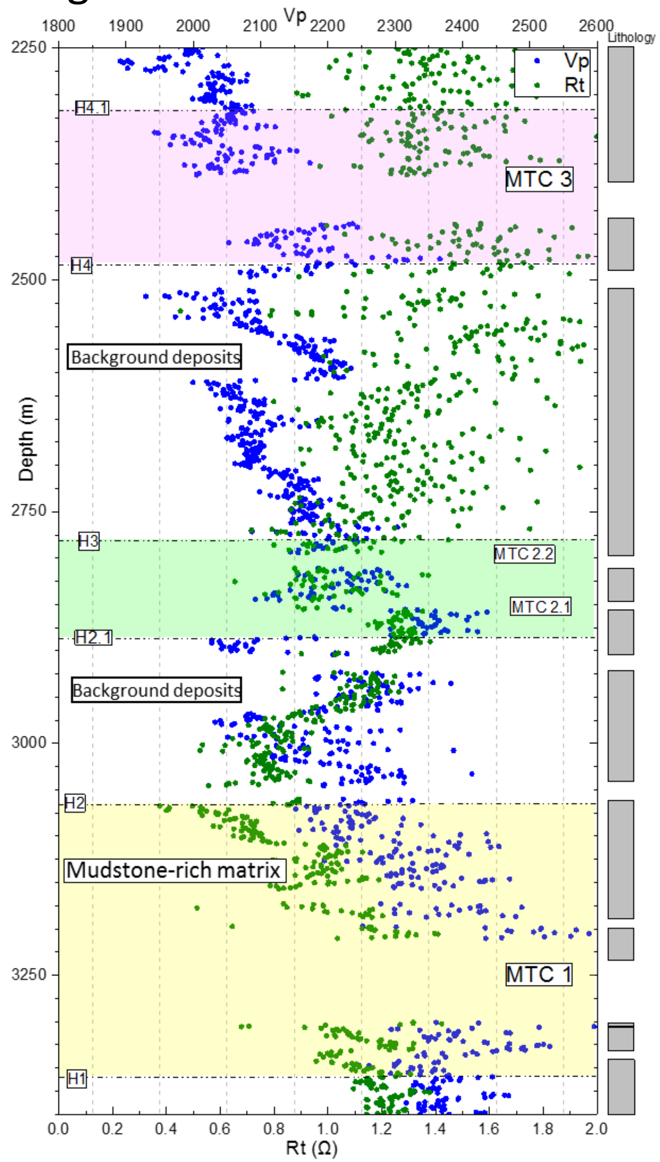

Figure 12B

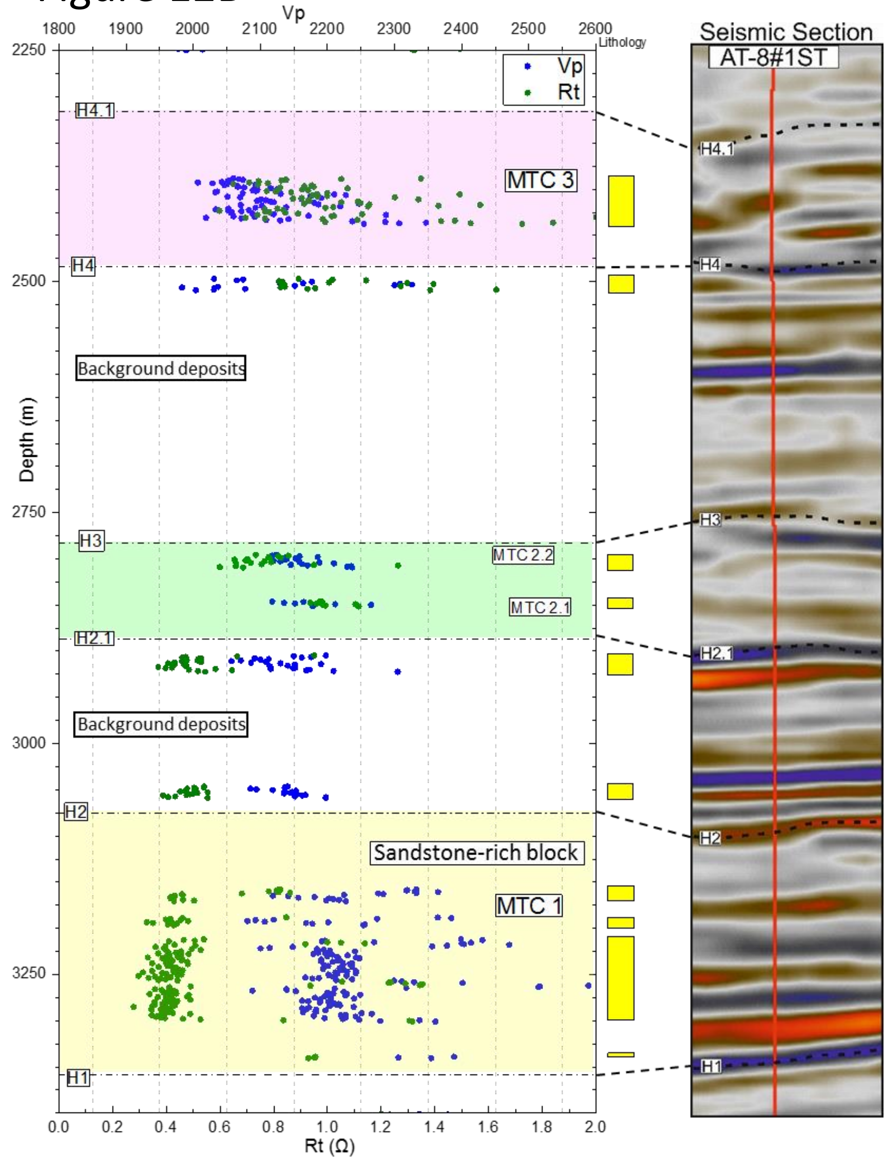

Figure 13A

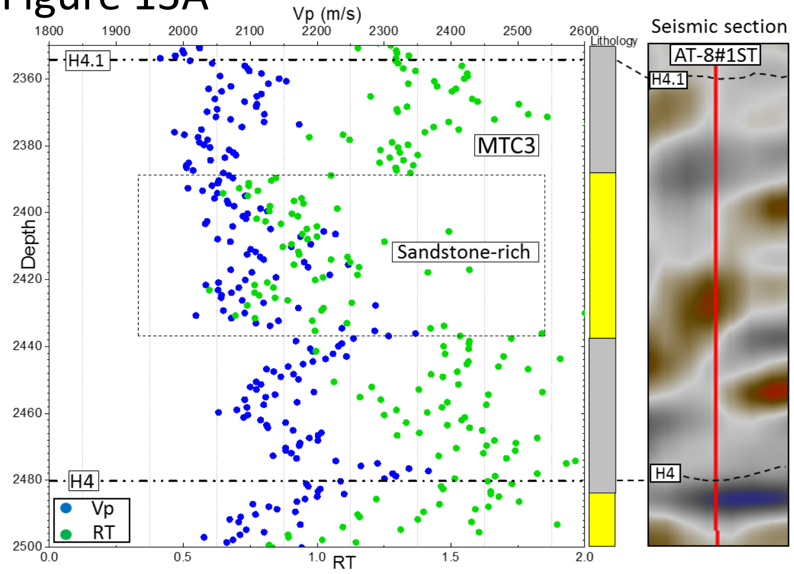

Figure 13B

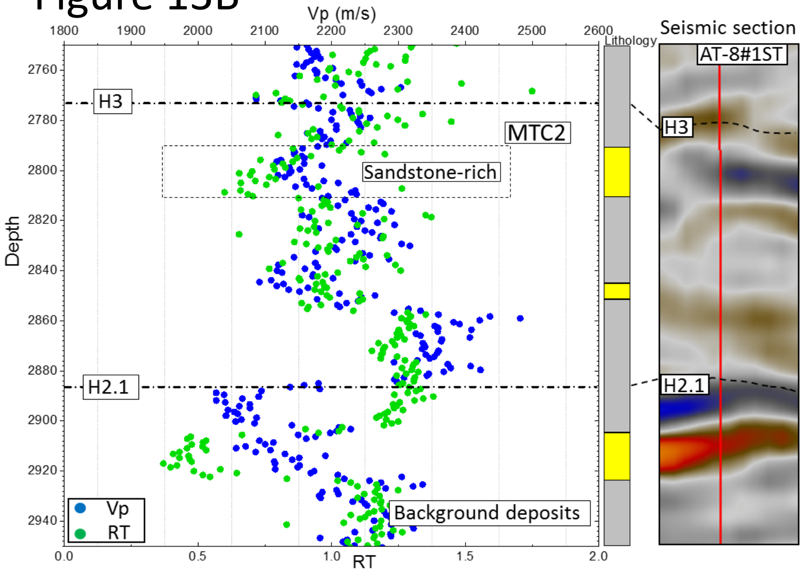

Figure 13C

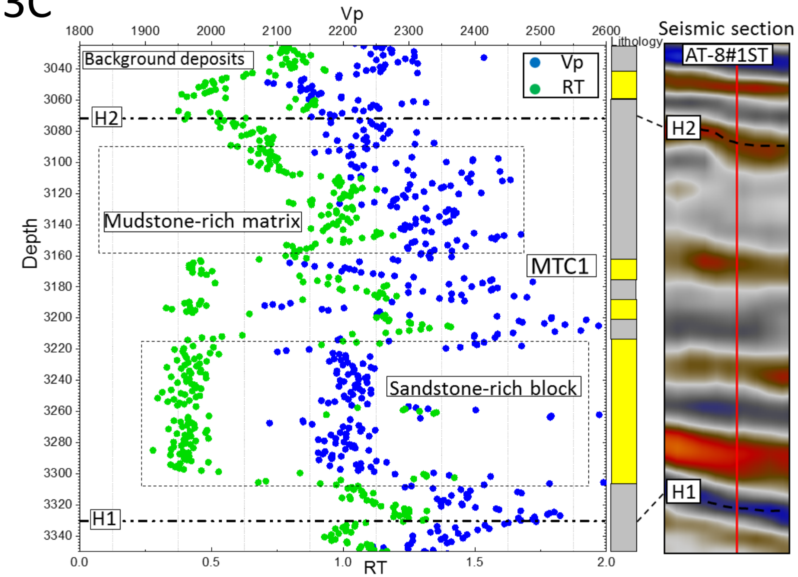

Figure 14

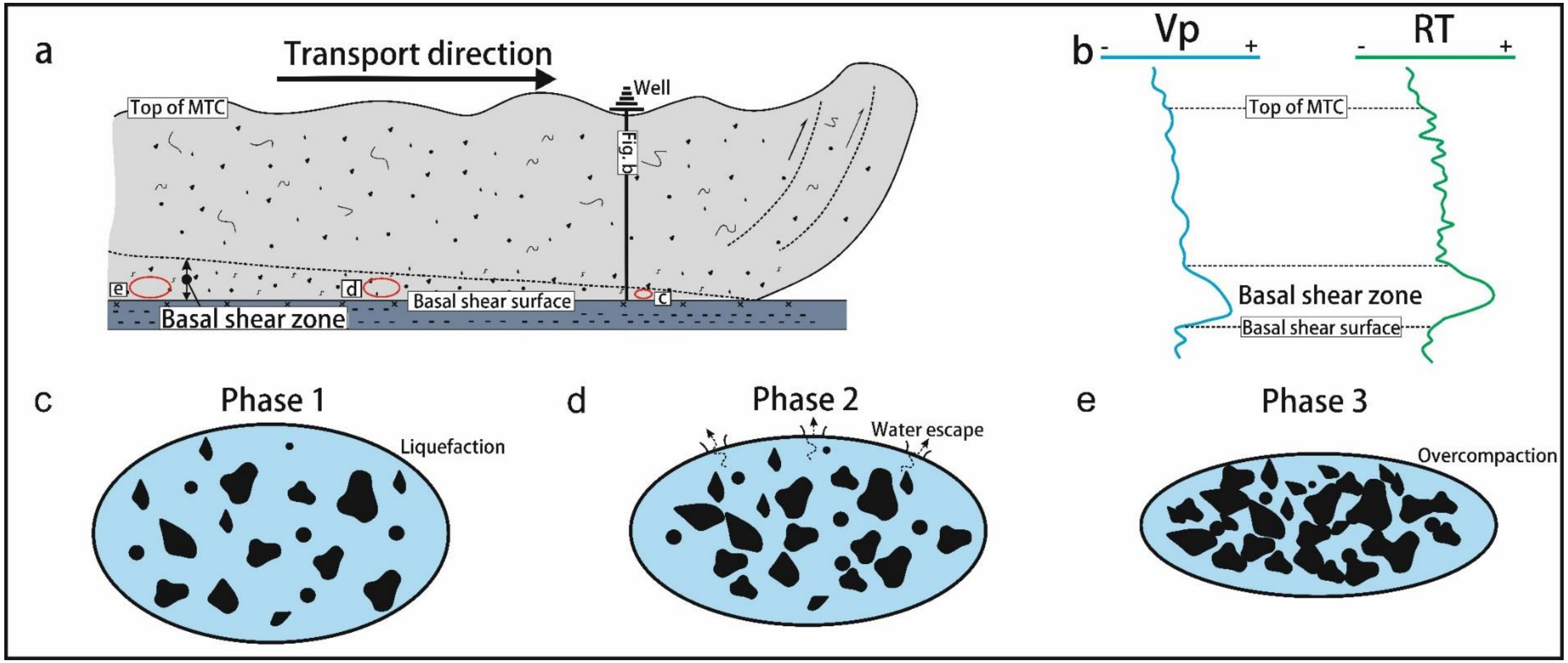

a
Transport direction
Well
Top of MTC
Fig. b
e
d
c
Basal shear surface
Basal shear zone
b
Vp
RT
Top of MTC
Basal shear zone
Basal shear surface
c
Phase 1
Liquefaction
d
Phase 2
Water escape
e
Phase 3
Overcompaction

Table 1

Seismic facies summary							
Types	***Seismic sections***	***GR*** (– +)	***Sonic*** (+ –)	***Lithology***	***Schematic facies geometries***	***Facies characteristics***	***Depositional enviroment***
SF1	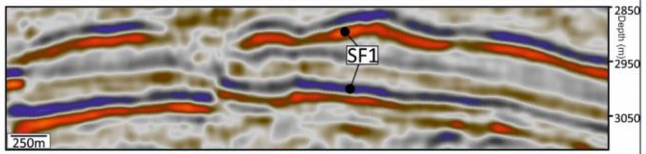		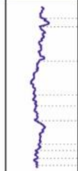	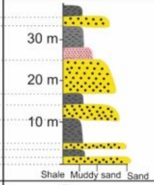	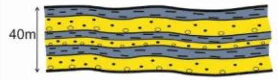	Sub-parallel to parallel, fair continuity, high amplitude reflections; seismic reflectors thinning and pitching out to the end. A fining up-ward trend with block low GR response at base and serrated high GR response at top.	Thinly bedded sandstone-rich and mudstone-rich deposits.
SF2	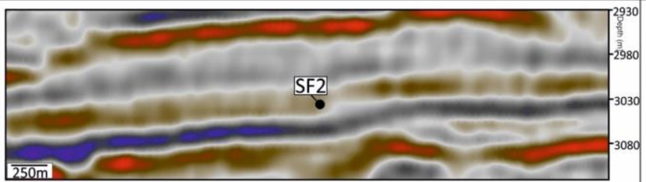			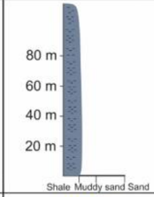	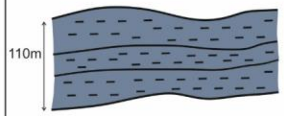	Sub-parallel to parallel reflections, good continuity, with medium to low amplitude reflections; Constantly serrated high GR response.	Background low energy mudstone-rich deposits.
SF3.1	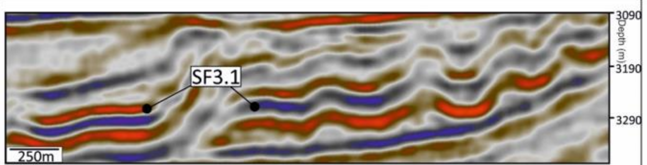			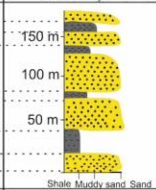		Less deformed, but more continuous, medium to high amplitude reflections; A fining upward trend GR response at base, a set of blocky low GR response at middle, and a fining upward GR response again at top.	Remobilised and transported sandstone-rich blocks
SF3.2	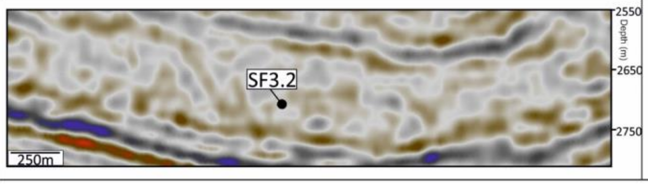			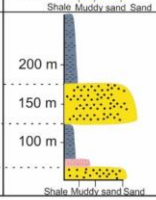	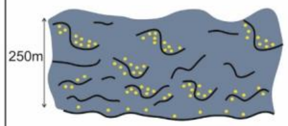	Chaotic reflections, bad continuity with medium to low amplitude reflections; Constantly serrated high GR response or high GR response interbedded with a set of blocky low GR response.	Mixed highly deformed slump deposits with large sandstone-rich blocks.

Table 2

MTC	Thickness (m)	Lithology	Thickness of sandstone rich parts (m)
MTC 1	270 m	Large sandstone-rich blocks with mudstone-rich debris	Approx. 180 m
MTC 2.1	77 m	Mudstone-rich debrite with sandstone-rich blocks	Approx. 30 m
MTC 2.2	43 m	Mudstone-rich debrite	Approx. 10 m
MTC 3	182 m	Mudstone-rich debrite with sandstone-rich blocks	Approx. 70 m